The other Higgses, at resonance, in the Lee-Wick extension of the Standard Model.

Prepared for submission to JHEP
CERN-PH-TH/2011-184
CP-3/2011-25

The other Higgses, at resonance, in the Lee-Wick extension of the Standard Model

Terrance Figy[a] **Roman Zwicky**[b]

[a] *TH Division, CERN, CH-1211 Geneva 23, Switzerland*
[b] *Southampton University, Highfield, SO17 1BJ Southampton, UK*

E-mail: terrance.maynard.figy@cern.ch, r.zwicky@soton.ac.uk

Abstract: Within the framework of the Lee Wick Standard Model (LWSM) we investigate Higgs pair production $gg \to h_0 h_0$, $gg \to h_0 \tilde{p}_0$ and top pair production $gg \to \bar{t}t$ at the Large Hadron Collider (LHC), where the neutral particles from the Higgs sector (h_0, $\tilde{h}_0$ and $\tilde{p}_0$) appear as possible resonant intermediate states. We investigate the signal $gg \to h_0 h_0 \to \bar{b}b\gamma\gamma$ and we find that the LW Higgs, depending on its mass-range, can be seen not long after the LHC upgrade in 2012. More precisely this happens when the new LW Higgs states are below the top pair threshold. In $gg \to \bar{t}t$ the LW states, due to the wrong-sign propagator and negative width, lead to a dip-peak structure instead of the usual peak-dip structure which gives a characteristic signal especially for low-lying LW Higgs states. We comment on the LWSM and the forward-backward asymmetry in view of the measurement at the TeVatron. Furthermore, we present a technique which reduces the hyperbolic diagonalization to standard diagonalization methods. We clarify issues of spurious phases in the Yukawa sector.

Keywords: Beyond the Standard Model

ArXiv ePrint: YYMM.NNNN

Contents

August 19, 2011 — 0:10

1 Introduction

1.1 The Lee-Wick Standard Model

The investigation of the mechanism of electroweak symmetry breaking (EWSB), responsible for the generation of fermion and gauge boson masses, is one of the primary tasks of the Large Hadron Collider (LHC) at CERN. The scalar Higgs particle realizes this mechanism in the Standard Model (SM), in a rather efficient way, at the expense of divergences quadratic in the cut-off. The latter fact, known as the hierarchy problem, is taken as an indication of the incompleteness of the SM and is at the heart of many models beyond the SM (BSM). An example of which is the Lee-Wick SM (LWSM) [1] where ideas to soften ultraviolet (UV) divergences in QED from the seventies [2, 3] were extended to chiral fermions and non-abelian gauge theories [1]. Most importantly it was shown that the LWSM is renormalizable and free from quadratic divergences [1] thus joining the list of models addressing the hierarchy problem successfully. In LW field theories higher derivative (HD) terms are added and terms quadratic in the fields are resummed into the propagator rather than treated as perturbations, ameliorating the UV behavior of perturbation theory. This results in additional poles in the propagators for which auxiliary fields (AF) can be introduced to cast the theory in terms of interactions with mass dimension no greater than four[1]. The additional fields are interpreted as LW partner states and do have the wrong-sign propagator, aka Pauli-Villars regulators. The key idea of Lee and Wick is that the LW ghost particles never appear as asymptotic states in detecters, nowadays reminiscent of the Faddev-Poppov ghosts in non-abelian gauge field theories. The connected issues of unitarity and causality which were debated in the seventies, e.g. the Erice lectures [4, 5], and reconsidered recently in [6]. Most notably the width becomes negative and requires a deformation of the contour to avoid new cuts [7] which assure no new asymptotic states. The status of LW field theories is that there are no known counterexamples to unitarity in perturbation theory up to today and that causality can be violated but only at distances below $M_{\rm LW}^{-1}$. It has been suggested that the violation of causality can be tested at the LHC [8]. The usual non-perturbative formulation via the path-integral seems difficult [9] but recently a restrictive path-integral was proposed where the contour prescription can be derived [10, 11].

Further conceptual issues of phenomenological nature have been investigated such as the behaviour at high temperature [12], unitarity of massive LW vector boson scattering [13], the compatibility of the see-saw and the absence of quadratic divergences [14], the running of couplings [15], UV-properties of LW field theories [16], even higher derivative LW field theories [17, 18] and LW fields and gravity [19]. The cosmology of LW field theories has been investigated in [20]. Phenomenological studies include LHC and linear collider signals of LW gauge bosons [21, 22], flavour changing neutral currents [23], electroweak precision observables (EWPO) have been investigated in [24] and [25] where gauge boson and fermion masses are found to be constrained up to a few TeV.

[1] It is amusing that in the AF-formalism the LWSM seems fine tuned with respect to the hierarchy problem whereas this is not the case in the HD-formalism as a single term is added in each sector.

1.2 The Higgs-sector of the Lee-Wick SM

The LW Higgs sector has been investigated in [26–29]. The neutral part consists of the CP-even h_0, $\tilde{h}_0$, which are the SM-like and the LW-like Higgs boson, and the CP-odd LW-like scalar $\tilde{p}_0$. The SM as well as the LW Higgs sectors are not easy to constrain, neither indirectly through loops nor directly through signals. First for large Higgs masses the latter enters only logarithmically, rather than quadratically, at one-loop [30]. Second the Higgs couples via Yukawa terms to fermions and is therefore highly suppressed in di-lepton signals $h \to l^+ l^-$ [2].

A salient feature of the LWSM, at least in its minimal version [1], is that there's roughly a single new parameter per sector. It's the mass in the HD formalism which predicts all masses and couplings in the language of the AF formalism. In this respect the LWSM resembles so-called sequential SM extensions. The aim of this paper is to investigate the effect of a low lying Higgs sector, as a function of this single new parameter and the Higgs mass. We focus on channels, accessible at the LHC, where the additional Higgs appear as intermediate states at or close to resonance.

- *Higgs boson pair production* is beyond reach at the LHC in the SM [32]. In extensions of the SM its a different quest as particles, with appropriate couplings and masses above the two Higgs threshold, can enhance the cross section by orders of magnitude without contradicting current constraints [3]. We consider $gg \to h_0 h_0$ and $gg \to \tilde{p}_0 h_0$. We find that the cross section of the latter can be enhanced by roughly three orders of magnitude with respect to the SM for a sizable range of masses. That is to say if the LW Higgs is above the SM-like Higgs pair threshold and not to far above the top pair threshold, $2m_{h_0} < m_{\tilde{h}_0} \lesssim 1.5(2m_t)$. If the latter bound is approached top pair production becomes the main channel:

- *top pair production through gluon fusion* does not suffer from low cross sections and has already been observed at colliders. The cross section of the invariant mass of the top-pair M_{tt} has been identified as an attractive observable to see resonance effects through interference with the QCD-part a long time ago e.g. [34]. LW field theories have a very different pattern in that the wrong-sign propagator and width lead to a dip-peak rather than a peak-dip structure in the spectrum. It should be added that such effects can and do also appear in strongly coupled theories such as low energy QCD as discussed in section 4.

The paper is organized as follows: In section 2 we give an overview of the Higgs and quark sectors within the LWSM. In sections 3 and 4 we discuss Higgs pair and top pair production from a theory point of view. In section 4.1 we comment on the top forward-backward asymmetry in view of the current TeVatron results. In section 5 we

[2] This is why, in our opinion, the LW Higgs is not a candidate for the Wjj-excess at the TeVatron [31] as it should already have been seen in Wll-signal or Wbb-signal.

[3] A well-known example is minimal supersymmetric SM (MSSM) [33]. In fact the LWSM Higgs sector particle content corresponds to a type-II two Higgs-doublet model with a new LW Higgs mass scale as a single new parameter with $\tan\beta = 1$. The masses of the different Higgs particles are discussed in section 2.

present plots. In section 6 we investigate the signal $gg \to h_0 h_0 \to \bar{b}b\gamma\gamma$. In section 7 we conclude. In appendices A and B we present further details of amplitudes for Higgs pair and top pair production, respectively. In appendix C a method that reduces the hyperbolic diagonalization to standard techniques is presented. In appendices C.1 and C.2 we present tree-level mass sum rules. Further, we clarify the issue of spurious phases versus CP-violating phases in the fermion mass matrices.

2 The Lee Wick Standard Model

We shall discuss the Higgs and Yukawa sectors directly in the auxiliary field formalism and refer the interested reader to [1] for the connection with the higher derivative formalism.

2.1 Higgs sector

The Lagrangian of the Higgs sector in the auxiliary field formalism assumes the following form [1]:

$$\mathcal{L} = (\hat{D}_\mu H)^\dagger (\hat{D}^\mu H) - (\hat{D}_\mu \tilde{H})^\dagger (\hat{D}^\mu \tilde{H}) + M_H^2 \tilde{H}^\dagger \tilde{H} - V(H - \tilde{H}) \,, \tag{2.1}$$

where $\hat{D}_\mu = \partial_\mu + i(\mathbf{A}_\mu + \tilde{\mathbf{A}}_\mu)$ with $\mathbf{A}_\mu = g A_\mu^a T^a + g_2 W_\mu^a T^a + g_1 B_\mu Y$ for SM gauge fields and analogously for the LW gauge boson for $\tilde{\mathbf{A}}_\mu$. The Higgs potential is $V(H) = \lambda/4(H^\dagger H - v^2/2)^2$. The mass M_H is the mass scale of the higher derivative LW mass scale. In the unitary gauge the two doublets are

$$H^\top = \left[0, (v + h_0)/\sqrt{2}\right] \,, \quad \tilde{H}^\top = \left[\tilde{h}_+, (\tilde{h}_0 + i\tilde{p}_0)/\sqrt{2}\right] . \tag{2.2}$$

It is worthwhile to emphasize that, prior to mixing, the SM but not the LW CP-even neutral Higgs acquires a vacuum expectation value:

$$\langle h_0 \rangle = v \,, \quad \langle \tilde{h}_0 \rangle = 0 \,. \tag{2.3}$$

We note the standard abuse of notation in not denoting the massless as well as the massive Higgs field by h_0. With (2.2) the mass Lagrangian assumes the following form:

$$\mathcal{L}_{\text{mass}} = -\frac{\lambda}{4} v^2 (h_0 - \tilde{h}_0)^2 + \frac{M_H^2}{2} (\tilde{h}_0 \tilde{h}_0 + \tilde{p}_0 \tilde{p}_0 + 2\tilde{h}_+ \tilde{h}_-) \,. \tag{2.4}$$

We note the mixing between the Higgs scalar and its LW–partner. The neutral CP-even Higgs field can be diagonalized by a symplectic rotation:

$$\begin{pmatrix} h \\ \tilde{h} \end{pmatrix} = \begin{pmatrix} \cosh\phi_h & \sinh\phi_h \\ \sinh\phi_h & \cosh\phi_h \end{pmatrix} \begin{pmatrix} h_{\text{phys}} \\ \tilde{h}_{\text{phys}} \end{pmatrix} \,. \tag{2.5}$$

for which the masses of the Higgs sector are given by,

	h_0	$\tilde{h}_0$	$\tilde{p}_0$	$h_\pm$
CP	even	even	odd	none
$\frac{m^2_{\text{phys}}}{M_H^2}$	$\frac{1}{2}\left(1 - \sqrt{1 - 2v^2\lambda/M_H^2}\right)$	$\frac{1}{2}\left(1 + \sqrt{1 - 2v^2\lambda/M_H^2}\right)$	1	1

(2.6)

and for completeness we have indicated the CP quantum numbers as well. For obtaining Feynman rules in terms of the physical masses the following relations are useful [26]:

$$\lambda v^2 = \frac{2m^2_{h_0,\text{phys}}}{(1+r^2_{h_0})}\,, \qquad r_{h_0} \equiv \frac{m_{h_0,\text{phys}}}{m_{\tilde{h}_0,\text{phys}}}\,, \tag{2.7}$$

and

$$\begin{aligned} s_H &= \cosh\phi_h = \frac{1}{(1-r^4_{h_0})^{1/2}}\,, \\ s_{H-\tilde{H}} &= \cosh\phi_h - \sinh\phi_h = \frac{1+r^2_{h_0}}{(1-r^4_{h_0})^{1/2}}\,. \end{aligned} \tag{2.8}$$

2.2 Yukawa Interactions

In order to discuss the Yukawa terms, it is helpful to first discuss the fermions. We shall closely follow ref. [26]. However, we choose a slightly different basis for the fermions and refer the reader to appendix C where a method is outlined how the hyperbolic diagonalization can be performed using standard tools.

The kinetic term of the AF Lagrangian is given by:

$$\mathcal{L} = \overline{\Psi^t} i\eta_3 \hat{\not{D}} \Psi^t - \overline{\Psi^t_R}\mathcal{M}_t\eta_3\Psi^t_L - \overline{\Psi^t_L}\eta_3\mathcal{M}^\dagger\Psi^t_R\,, \tag{2.9}$$

with

$$\Psi^{t\top}_L = (T_L, \tilde{t}'_L, \tilde{T}_L)\,, \qquad \Psi^{t\top}_R = (t_R, \tilde{t}_R, \tilde{T}'_R)\,, \tag{2.10}$$

where all capitalized components are part of an SU(2) doublet; e.g. $Q_L = (T_L, B_L)^\top$. It is noteworthy that a chiral fermion necessitates two chiral fermions which in turn form a massive Dirac fermion. This becomes explicit in the basis chosen above

$$\mathcal{M}_t\eta_3 = \begin{pmatrix} m_t & 0 & -m_t \\ -m_t & -M_u & m_t \\ 0 & 0 & -M_Q \end{pmatrix}\,, \qquad \eta_3 = \begin{pmatrix} 1 & 0 & 0 \\ 0 & -1 & 0 \\ 0 & 0 & -1 \end{pmatrix} \tag{2.11}$$

which differs from the one in [26]. Note though that all physical masses remain unchanged under change of basis. The mass matrix is diagonalized by symplectic rotations S_L and S_R:

$$\Psi_{L(R),\text{phys}} = \eta_3 S^\dagger_{L(R)}\eta_3\Psi_{L(R)}\,, \qquad \mathcal{M}_{t,\text{phys}}\eta_3 = S^\dagger_R\mathcal{M}_t\eta_3 S_L\,, \tag{2.12}$$

which leave the kinetic terms invariant by virtue of

$$S_L\eta_3 S^\dagger_L = \eta_3 \quad \text{and} \quad S_R\eta_3 S^\dagger_R = \eta_3\,. \tag{2.13}$$

Now we may turn to the Yukawa sector for which we only write down the neutral Higgs part:

$$\mathcal{L} = -\frac{1}{v}(h_0 - \tilde{h}_0)\left(\overline{\Psi^t_R}g_t\Psi^t_L + \overline{\Psi^t_L}g^\dagger_t\Psi^t_R\right) - \frac{1}{v}(-i\tilde{p}_0)\left(\overline{\Psi^t_R}g_t\Psi^t_L - \overline{\Psi^t_L}g^\dagger_t\Psi^t_R\right)\,, \tag{2.14}$$

where the g matrix has non-diagonal entries which allow for transitions between LW-generations and is given in the initial and physical basis by:

$$g_t = \begin{pmatrix} m_t & 0 & -m_t \\ -m_t & 0 & m_t \\ 0 & 0 & 0 \end{pmatrix} , \quad g_{t,\text{phys}} = S_R^\dagger g_t S_L \, . \tag{2.15}$$

3 Higgs boson pair production

We shall parametrize the $gg \to h_0 h_0$ matrix element as follows:

$$\mathcal{M}(gg \to h_0 h_0) = \frac{1}{32\pi^2} \delta^{ab} \frac{g^2}{v^2} \Big(\mathcal{A}_0 P_0 + \mathcal{A}_2 P_2 \Big)_{\mu\nu} e(p_1)^\mu_a \, e(p_2)^\nu_b \, , \tag{3.1}$$

with analogous conventions for $gg \to \tilde{p}_0 h_0$. The pre-factor arises as follows: $1/2\delta^{ab}$ due to the colour trace, $1/4$ from perturbative expansion, the fraction g^2/v^2 from the couplings of the vertices and $1/(4\pi^2)$ is factored out in order to give simple results for the amplitudes. The parity-even projectors on gluon spin 0 and 2, P_0 and P_2, as well as their parity-odd counterparts, $\tilde{P}_0$ and $\tilde{P}_2$, are defined in appendix A. The parton cross section for $2 \to 2$ scattering process for two massless incoming particles is given by $1/(16\pi\hat{s}^2)|\mathcal{M}|^2$ [36] and averaging over initial state polarizations $1/4$ and colour $1/(N_c^2-1)^2 = 1/64$ one arrives at[4]:

$$\frac{d\hat{\sigma}(gg \to h_0 h_0)}{d\hat{t}} = \frac{1}{2^{19}} \frac{1}{\pi^5} \frac{g_s^4}{v^4} \left(|\mathcal{A}_0|^2 + |\mathcal{A}_2|^2 \right) \tag{3.2}$$

This result is for identical particles. In the case the particles in the final state are not identical one has to multiply by a factor of two[5]. The spin 0 amplitudes, parity-even and odd, receive contributions from the triangle and box diagrams, c.f. figure 1(left) and (right) respectively, whereas the spin 2 amplitudes only receive contributions from the box diagrams:

$$\mathcal{A}_0 = \mathcal{A}_0^\triangle + \mathcal{A}_0^\square \, , \quad \mathcal{A}_2 = \mathcal{A}_2^\square \quad . \tag{3.3}$$

For what follows it is important to notice that the gluon-quark vertex is diagonal in LW-generation space whereas the Higgs-quark vertex is not (2.14). Since, the Higgs-quark vertex does not contribute to the triangle graph the latter can be obtained from the SM with simple corrections for vertices as described in appendix A.1. The modification of the box graphs are twofold. First, the external Higgs particles are modified by the mixing factor $s^2_{H-\tilde{H}}$ as for the triangle. Second, one has to take into account that at the Higgs-quark vertex the LW-generations mix (2.14) as discussed above. We find that these modifications

[4] This agrees with [37] with the following identifications: $|\mathcal{A}_0|^2 = |\text{gauge1}|^2$ and $|\mathcal{A}_2|^2 = |\text{gauge2}|^2$ at the difference that here $\mathcal{A}_{0,2}$ are meant to include the LW contributions as well.

[5] We have thus implicitly assumed that the variable t is understood to be integrated over its entire domain despite the Bose symmetry in the identical particle case.

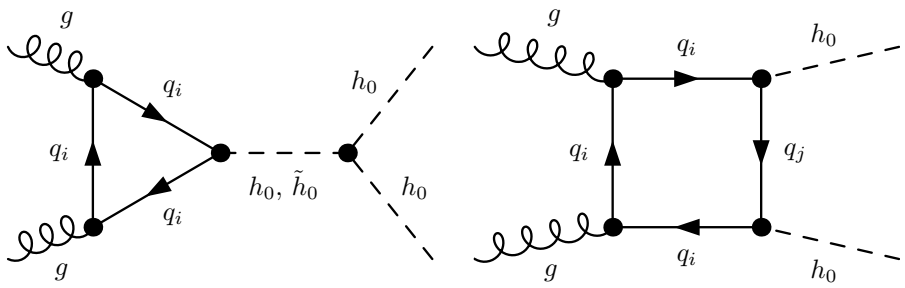

(a) (b)

Figure 1. (a) Triangle graphs for $q = (t, \tilde{t}, \tilde{T}, b, \tilde{b}, \tilde{B})$ and (b) one out of six box graphs for $q_i, q_j = (t, \tilde{t}, \tilde{T}, b, \tilde{b}, \tilde{B})$.

are most efficiently presented as follows:

$$\mathcal{A}_0^{\square}(gg \to h_0 h_0) = s^2_{H-\tilde{H}} \sum_{i,j=1}^{3} \left(f_{11}(i,j) + f_{55}(i,j) \right)$$
$$\tilde{\mathcal{A}}_0^{\square}(gg \to h_0 \tilde{p}_0) = -i s_{H-\tilde{H}} \sum_{i,j=1}^{3} \left(\tilde{f}_{15}(i,j) + \tilde{f}_{51}(i,j) \right) , \tag{3.4}$$

where

$$f_{XX}(i,j) = \sum_{f}^{\text{flavours}} [\eta_3 \, S(X)_f]_{ij} [\eta_3 \, S(X)_t]_{ji} (a_0)^{\square}_{XX}(m_i, m_j)]$$
$$\tilde{f}_{XY}(i,j) = \sum_{f}^{\text{flavours}} [\eta_3 \, S(X)_f]_{ij} [\eta_3 \, P(Y)_f]_{ji} (\tilde{a}_0)^{\square}_{XY}(m_i, m_j)] \, . \tag{3.5}$$

In regard to the formulae (A.17) it is important to notice that the h_0 and $\tilde{p}_0$ are associated with the the momenta p_3 and p_4 respectively as can be inferred from the formula in appendix A.2. The couplings $S(P)_{X,Y}$, which follow from eq. (2.14), are:

$$S(1)_t = \frac{1}{2}(g_t^\dagger + g_t) \, , \qquad S(5)_t = \frac{1}{2}(g_t^\dagger - g_t) \, ,$$
$$P(1)_t = \frac{1}{2}(-g_t^\dagger + g_t) \, , \quad P(5)_t = \frac{1}{2}(-g_t^\dagger - g_t) \, , \tag{3.6}$$

where the top flavour was chosen as a representative and the subscript phys has been omitted on the Yukawa couplings for the sake of notational brievety. The $\eta_3 = \text{diag}(1, -1, -1)$ matrices take care of the signs of the SM and LW propagators respectively and the couplings $g_{X,Y}$ govern the LW-generation transitions. The spin 2 structures $\mathcal{A}_2^{\square}$ and $\tilde{\mathcal{A}}_2^{\square}$ are completely analoguous.

4 Top pair production

In this section we discuss the interference between the QCD background and resonant particles in top pair production in a qualitative manner.[6] In the LWSM potential resonant particles, that couple to the top triangle loop and decay into top pairs are the h_0, $\tilde{h}_0$, $\tilde{p}_0$, Z and $\tilde{Z}$ corresponding to the diagrams shown in figure 1(a) and figure 12(a,b,c), respectively, with the Higgs final states replaced by top pairs. Here we shall neglect the Z and the $\tilde{Z}$ as the former is far off-shell at $s > 2m_t$ and the latter is severely constrained by di-lepton searches to be heavier than 1 TeV and by electroweak precision measurement to be in the multi-TeV range. The corresponding amplitudes, which consist of triangle graphs only, are easily obtained from the one for Higgs-production and are given in appendix B.

The interference effect of an intermediate resonance $gg \to R \to \bar{t}t$, where R stands for a generic resonance, takes the following form [34]:

$$\begin{aligned}\frac{d\hat{\sigma}}{ds}(gg \to \bar{t}t)|_{\text{interference}} &= -|c(s)|\text{Re}\left[\frac{l_\triangle}{s - m_R^2 + im_R\Gamma_R}\right] \\ &= -|\tilde{c}(s)|\left((s - m_R^2)\text{Re}[l_\triangle] + m_R\Gamma_R\text{Im}[l_\triangle]\right) \ , \end{aligned} \tag{4.1}$$

where $l_\triangle = l_\triangle(s/4m_t^2)$ is the appropriate triangle loop function, $c(s)$ is a well-known function of s [34], $\tilde{c}(s)$ differs from $c(s)$ by a constant and s the invariant mass of the two gluons entering the loop. If there is no loop function then the term above will lead to a peak-dip structure passing from constructive to destructive interference at $s = m_R^2$. The loop-function does not change this pattern in the case where the resonance is a scalar or a pseudoscalar [34] as the real and imaginary part of the loop function are positive. The pattern persists for a spin-1 particles as well as can be inferred from the plots in reference [44]. Thus the question what happens in the LW case. Due to the negative sign of the propagator and the width,

$$\begin{aligned}\frac{d\hat{\sigma}}{ds}(gg \to \bar{t}t)|_{\text{LW}-\text{interference}} &= -|c(s)|\text{Re}\left[\frac{-l_\triangle(s/4m_t^2)}{(s - m_R^2) - im_R\Gamma_R}\right] \\ &= -|\tilde{c}(s)|\left(-(s - m_R^2)\text{Re}[l_\triangle] + m_R\Gamma_R\text{Im}[l_\triangle]\right) \ , \end{aligned} \tag{4.2}$$

the $(s - m_R^2)\text{Re}[l_\triangle]$ term flips sign[7]. Assuming that neither the width nor the imaginary part of the loop function $l_\triangle$ are anomalously large, this leads to a dip-peak structure. In fact the passage from destructive to constructive interference, which we shall call $\mathcal{M}_R$, does not coincide with the exact location of the resonance:

$$\mathcal{M}_R^2 = m_R^2 + \frac{\text{Im}[l_\triangle]}{\text{Re}[l_\triangle]} m_R\Gamma_R \tag{4.3}$$

Examples of the effect are shown in figure 2. The dip-peak structure is a unique feature

[6] We note that in ref. [35] the authors explored these types of interferences in the context of minimal supersymmetric standard model and Little Higgs models.

[7] It is crucial that the intermediate resonance couples to the tops from the loops and the final state tops as otherwise a minus could be absorbed in either one of the couplings.

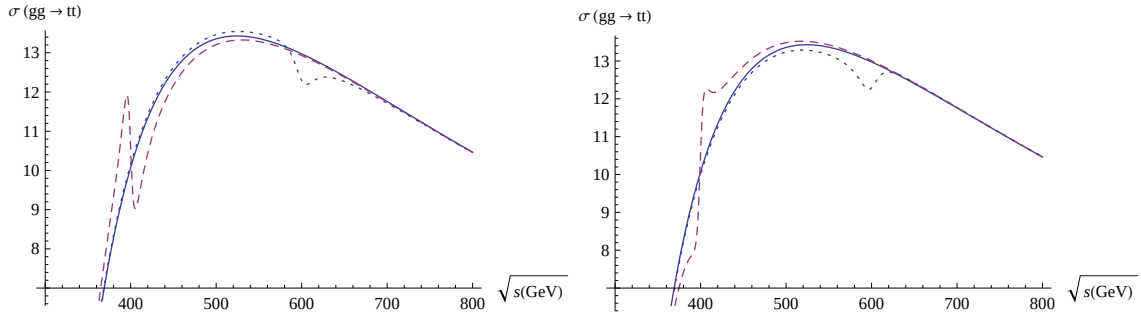

Figure 2. The cross section $\sigma(gg \to \bar{t}t)$ as taken from [34] qft with energy dependent width. The solid line is the LO QCD contribution. The dashed(dotted) lines correspond to a resonance mass $m_R = 400(600)$, GeV. The left(right) figure corresponds to the usual (LW) resonance-type.

of LW field theories, produced via gluon fusion through the top triangle, in the case of a well isolated resonance. We would like to add to that in the case where the masses of two resonances are close to each other their mixing has to be taken into account by the so-called K-matrix formalism e.g. [45]. It is important to realize that a dip-peak structure is present in the π-π-scattering spectrum for the $f_0(980)$ meson due to the extremely broad $f_0(600)$ (σ-meson) [46]. Thus strongly coupled extensions of the SM, such as technicolor, might have similar signals as the LWSM.

4.1 A comment on the top forward backward asymmetry

Currently, the top forward-backward asymmetry (tAFB), $A_{\rm FB}^{\bar{t}t} = 0.475(114)$ for $M_{tt} > 450\,\text{GeV}$ at [47] at $5.3\,\text{fb}^{-1}$, deviates from SM prediction $A_{\rm FB}^{\bar{t}t} = 0.088(13)$ [47] at about the 3σ-level at the TeVatron[8]. The SM prediction originates from a charge asymmetry which, due to the fact that the TeVatron is a $p\bar{p}$-collider, translates into a forward-backward asymmetry. Thus the question is whether the LWSM has the potential to explain this discrepancy. A nice summary of perturbative approaches to the tAFB is given in reference [49]. The LWSM qualifies at the same level as a Z'-model with SM-like couplings, where the role of the Z' is taken by $\tilde{Z}$.[9] We roughly get $A_{\rm FB}^{\bar{t}t} \simeq 0.01$, for a $m_{\tilde{Z}} = 1\,\text{TeV}$, at best which is in the right direction but too small to join into the current excitement.[10] Note, as only the absolute value of the propagator enters, the wrong-signs of the propagator and the width do not matter. We have not evaluated the interference of the $\tilde{Z}$ and the SM Z, but expect it to be of similar size.

5 Numerical results

We compute cross sections for $pp \to h_0 h_0/\tilde{p}_0 h_0$ and the differential cross section $pp \to \bar{t}t$ via gluon fusion at the LHC for $\sqrt{S} = 7/14$ TeV respectively[11]. We denote the pp center of mass

[8] The very recent D0-results at $5.4\,\text{fb}^{-1}$ is much closer to the SM value [48].

[9] The LWSM does not qualify as an axi-gluon, nor are there large flavour changing couplings between the first and third generation in its minimal version.

[10] Note $m_{\tilde{Z}} = 1\,\text{TeV}$ is even a bit low in regard to electroweak precision data [24].

[11] The cross section for vector boson fusion $qq \to h_0 h_0 jj$ is about 2% of $gg \to h_0 h_0$ and thus negligible.

energy by capital S and the partonic center of mass energy by lower case s throughout this paper. The renormalization and factorization scale has been chosen to be $\mu_r = \mu_f = 2m_{h_0}$ for $pp \to h_0 h_0$ and $\mu_r = \mu_f = m_{h_0} + m_{\tilde{p}_0}$ for $pp \to \tilde{p}_0 h_0$. We use the MSTW 2008 LO (90% C.L.) for parton distribution functions with the strong coupling calculated to one-loop order for $\alpha_s(m_Z) = 0.13939$ [50]. We use LO predictions for $gg \to h_0 h_0/\tilde{p}_0 h_0$. The NLO corrections in the later case are rather large [51]; almost 100% as can be inferred from figure 6 of that reference. Fortunately, the shape of the corrections are almost identical to the LO result and thus should not distort the analyses too much. For $gg \to \bar{t}t$ we also use LO predictions with the factorization scale set to $\mu_f = m_t$ and the renormalization scale set to $\mu_r = m_t(m_\phi)$ for $gq\bar{q}$ ($gg\phi$ for $\phi = \tilde{p}_0, \tilde{h}_0, h_0$) couplings for which we comment in section 4.

For the numerical computations we have used various computer packages to be referred to below. The FeynArts [52] model file has been generated automatically using LanHEP [53]. The resulting model files were modified to allow for wrong-sign propagators in the auxiliary field formalism. Fortran code for the cross sections was generated with the use of FormCalc [54]. All loop integrals were computed using LoopTools [54].

The width-mass ratios, widths and branching ratios for h_0 and $\tilde{h}_0$ are depicted in appendix A.5. in figures 13,14(left) and 15 respectively. They will be referred throughout and serve to understand the results qualitatively. Possibly the most important aspect for further understanding is that the width of the $\tilde{h}_0$ (in figure 14(left) appendix A.5) raises significantly when the $t\bar{t}$-threshold is crossed (in parameter-space $m_{\tilde{h}_0} > 2m_t$) and is relevant for the triangle diagrams with intermediate $\tilde{h}_0$.

5.1 Contraints on LW mass scales

Before presenting the main results the new LW scales have to be discussed. There are six LW mass scales plus the mass of the SM-like Higgs boson out of which five are constrained to be rather high and generally do not impact on our investigation The parameters are:

- The scales M_1 and M_2 of the LW gauge bosons associated with $\mathrm{U}(1)_Y$ and $\mathrm{SU}(2)_L$ are constrained by electroweak precision measurements to be in the multi-TeV range [24]. We shall set $M_1 = M_2 = 1\,\mathrm{TeV}$ throughout this paper as in this range the masses have no major influence on our results.

- The fermion mass scales M_Q, M_u and M_d [12] are constrained through loop-contributions to electroweak precision measurements to be in the multi-TeV range [25]. For the $gg \to h_0 h_0$ channel the fermion mass scale has little influence for $M_Q = M_u = M_d > 500\,\mathrm{GeV}$ as can be inferred from the appendix A.5 figure 16. There are no qualitative changes when one goes away from the limit of equal masses and we therefore assume the the fermion mass scales to be $500\,\mathrm{GeV}$ in the plots. For the $gg \to \tilde{p}_0 h_0$ channel there are some threshold effects due to the box diagrams.

[12] Due to chiral suppression, only heavy flavours are relevant. This statement can be inferred from the HD formalism. Thus only the top and the beauty quarks are taken into consideration.

- The masses of the two neutral CP-even Higgses h_0 and $\tilde{h}_0$ (2.6). Every other parameter, in the Higgs sector, can be expressed in terms of these two. In particular the pseudoscalar mass, at tree-level satisfies (2.6)

$$m_{\tilde{p}_0}^2 = m_{h_0}^2 + m_{\tilde{h}_0}^2 \,, \tag{5.1}$$

  where we have dropped the subscript "phys" and shall do so in the remainder of this paper. The Higgs parameter-space has already been studied in other works. The collider analysis of $gg \to h_0 \to \gamma\gamma$ [26] was extended to final state channels γZ and WW in [29]. A part of the parameter-space has been found to be excluded by TeVatron results, c.f. figure 3 in that paper. It has to be added that this work was done in the narrow width approximation. Inspecting the plots in figure 13 it would seem that the effect of the width should be moderate in most of the parameter-space that has been excluded. The overlap of the interesting parameter-space and their excluded region is rather small and we leave it to the reader to convince him or herself of this fact. Using the correspondence of the the LWSM Higgs-sector and the type-II two Higgs doublet model mentioned, in the introduction, the effects of the charged Higgs boson $\tilde{h}_+$ on flavour physics were investigated in reference [27]. Using NLO predictions for $b \to s\gamma$, neglecting the influence of all other LW states, which is consistent with our analysis, it was found that $m_{\tilde{h}_+} > 463\,\text{GeV}$ at the 95% confidence level. Together with the tree-level relation (5.1) and $m_{\tilde{p}_0} = m_{h_+}$ (2.6) this sets a significant constraint on the lower range of our parameter space. Concerning this indirect bound there are two remarks to be made. First, the individual theoretical uncertainties were added in quadrature, which is common practice, and thus the uncertainty might be considered to be a little bit on the low side. Second, the tree-level relation between the Higgs masses might receive significant radiative corrections due to the large top mass which is the case in the MSSM.

We would like to add that the limit of degenerate masses of the h_0 and $\tilde{h}_0$, parametrized by $r_{h_0} \equiv m_{h_0}/m_{\tilde{h}_0}$, is somewhat delicate. In connection with real particles, in the sense of parton level, it does not make sense to treat them separately. This can be seen in the pole in r_{h_0} in $s_{H-\tilde{H}} = (1 + r_{h_0}^2)(1 - r_{h_0}^4)^{-1/2}$. For virtual particles it is best to resort to the HD-formalism where everything should remain consistent. In regard to these points we disregard the parameter space where

$$r_{h_0} > 0.8 \,, \qquad r_{h_0} \equiv \frac{m_{h_0}}{m_{\tilde{h}_0}} \,, \tag{5.2}$$

which is somewhat more conservative than the value $r_{h_0} > 0.9$ chosen in [8]. It would be interesting to study these effects, from scratch, in the HD-formalism and find the relation to the K-matrix formalism [45] used to improve on two nearby Breit-Wigner resonances in usual field theory.

5.2 Results for $gg \to h_0 h_0$

The main point is that for $m_{\tilde{h}_0}$ slightly above $2m_{h_0}$ the cross section is large, three orders of magnitude larger than the one of the SM, dominated by the resonant contribution in the triangle graph figure 1(left). This is reminiscent of the situation in the MSSM [33].

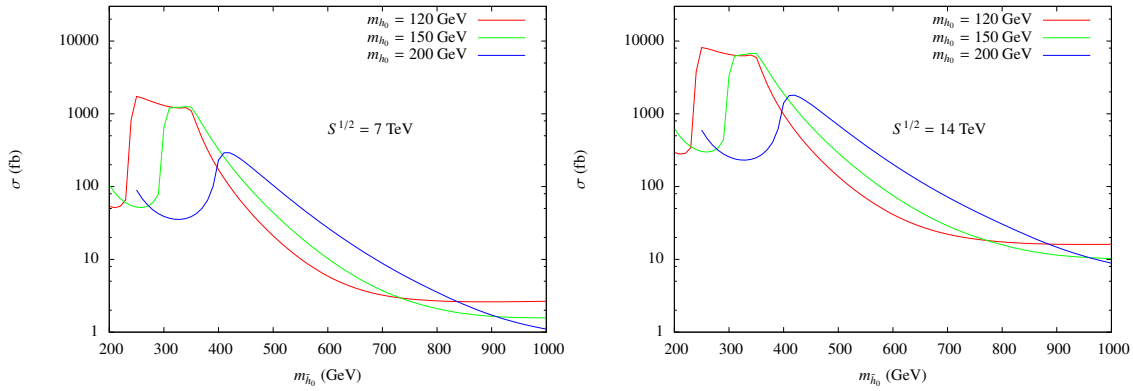

Figure 3. The cross section (in fb) for $gg \to h_0 h_0$ via gluon fusion at the LHC for $\sqrt{S} = 7/14$ TeV respectively versus the mass of the $\tilde{h}_0$, $m_{\tilde{h}_0}$, for three different values of m_{h_0}.

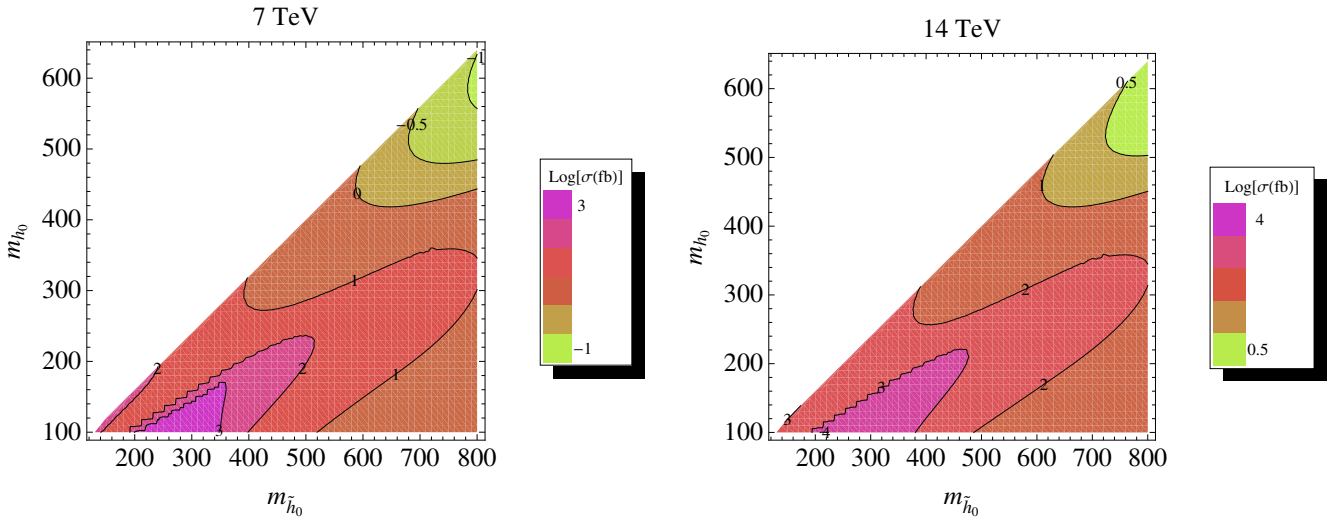

Figure 4. Contour plot of the total cross section (if fb) for $gg \to h_0 h_0$ ($\sqrt{S} = 7/14$ TeV respectively) versus the light Higgs boson mass, m_h and heavy Higgs boson mass, $m_{\tilde{h}}$ for $M_Q = 0.5$ TeV and $M_1 = M_2 = 1$ TeV. Note figure 3 corresponds to horizontal sections in this plot.

In figure 3 we show the total cross section for $gg \to h_0 h_0$ for $\sqrt{S} = 7/14$ TeV respectively as a function of $m_{\tilde{h}_0}$ for three different values of m_{h_0}. More detailed information can be inferred from the contour plots in the $(m_{h_0}, m_{\tilde{h}_0})$-plane shown in figure 4. As mentioned above one observes a sharp raise of the cross section when the LW Higgs mass crosses the threshold $2m_{h_0}$, c.f. figure 3. For higher $m_{\tilde{h}_0}$ the resonance contribution decouples and finally approaches the SM value. An interesting effect arises when the top threshold is reached. For the observation to be made below recall that the process is dominated by the triangle graph with an intermediate LW Higgs propagator of the form $(s - m^2_{\tilde{h}_0} - i m_{\tilde{h}_0} \Gamma_{\tilde{h}_0})^{-1}$. The slight dip in the branching ratio, c.f. figure 15(right), below the $t\bar{t}$-threshold results in a slight raise of the curve in case the where $m_{h_0} < m_t$. Once the $t\bar{t}$-threshold is reached the rapidly growing decay rate is damped through the additional relevant part in the prop-

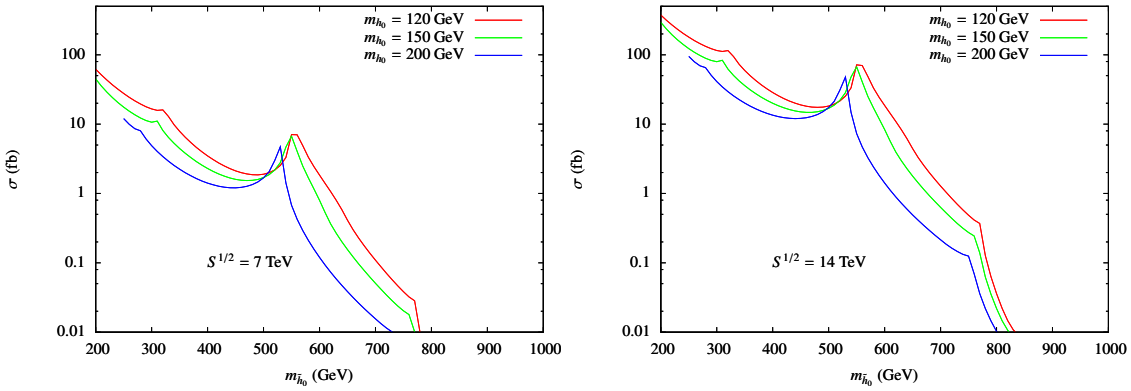

Figure 5. The cross section (in fb) for $pp \to h_0\tilde{p}_0$ via gluon fusion at the LHC for $\sqrt{S} = 7/14$ TeV respectively versus the mass of the $\tilde{h}_0$, $m_{\tilde{h}_0}$, for three different values of m_{h_0}. Note the kinks are due to crossing thesholds in corners of the box diagrams as described in the text; recall $M_Q = M_u = M_d = 500$ GeV.

agator. Note the lower part of the blue curve raises. In the HD-formalism this can be understood by the to the two poles m_{h_0} and $m_{\tilde{h}_0}$ approaching each other.

5.3 Results for $gg \to h_0\tilde{p}_0$

The cross section for $\sqrt{S} = 7/14\,\text{TeV}$ respectively with fixed m_{h_0} are shown in figure 5. The corresponding contour plots are shown in figure 6. The crucial difference to $gg \to \tilde{h}_0 \to h_0h_0$, in terms of the triangle diagram, is that there's no parameter region where there's a dominant resonance effect. The diagrams are shown in figure 12: the intermediate Z and $\tilde{Z}$ are either too light or too heavy respectively and the process $gg \to \tilde{p}_0 \to \tilde{p}_0h_0$ is not on-shell. There's a remnant of the latter effect when the m_{h_0} is relatively small and $p_0 \to \tilde{p}_0h_0$ approaches an on-shell configuration. The cross section is enhanced for $r_{h_0} \to 0.8$ (5.2) due a larger coupling $s_{H-\tilde{H}}$ of the SM-like Higgs to the two pseudoscalars. For large $m_{\tilde{h}_0}$ the cross section goes to zero which is consistent with the fact that this process is not present in the SM. We further note the thresholds in $2m_t$ and $m_t + m_{\tilde{t}}$ in the pseudoscalar mass, parametrized in terms of the CP-even Higgs masses according to eq. (5.1), become visible. These effects are not present in $gg \to h_0h_0$, since, the mass of the final state particles was assumed to be below these thresholds.

5.4 Results for $gg \to \bar{t}t$ (the M_{tt}-spectrum)

In this section we present the $\bar{t}t$-mass spectrum. In the case where the h_0 or $\tilde{p}_0$ are above the $\bar{t}t$-threshold ($m_{h_0}, m_{\tilde{p}_0} > 2m_t$) a dip-peak structure is to be expected, originating from the interference of the QCD-background with LW Higgs states, as described in section 4. This phenomenon is observed in the actual simulation as can be inferred from figure 7 for $m_{h_0}, m_{\tilde{h}_0} = (125, 450)\,\text{GeV}$ but is hard to see for higher values of LW Higgs mass e.g. $m_{h_0}, m_{\tilde{h}_0} = (125, 800)\,\text{GeV}$. This is because the width of the intermediate $\tilde{h}_0$ and $\tilde{p}_0$ becomes large and the two terms in eq.(4.2) tend to cancel each other. In the latter case the signal to background ratio can be improved significantly in the case where a p_T-cut of

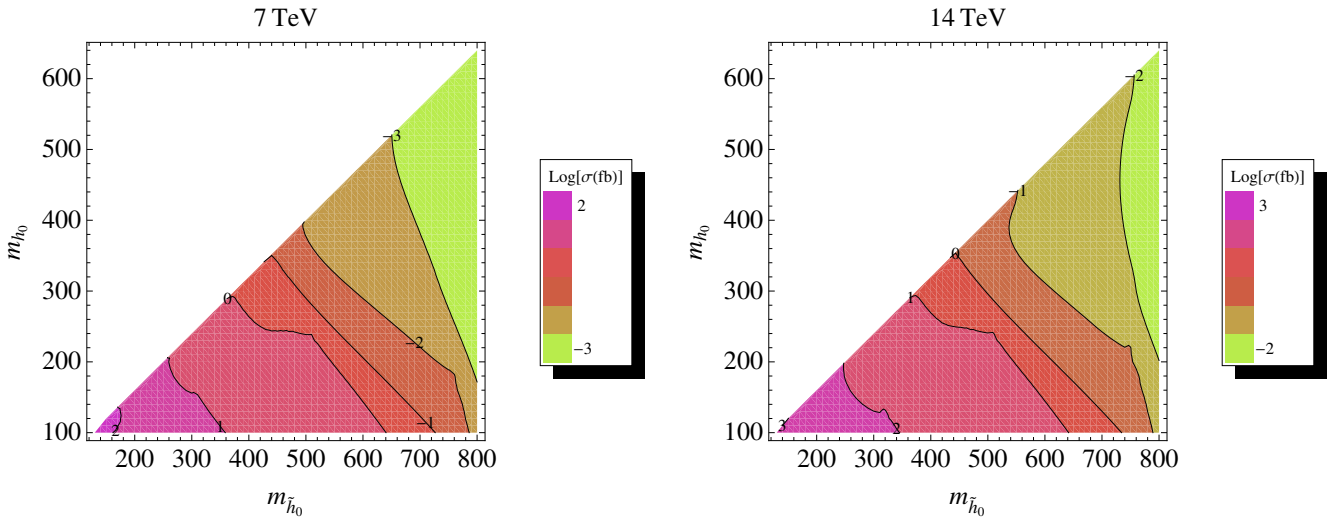

Figure 6. Contour plot of the total cross section (in fb) for $gg \to h_0\tilde{p}_0$ ($\sqrt{S} = 7/14$ TeV respectively) versus the light Higgs boson mass, m_h and heavy Higgs boson mass, $m_{\tilde{h}}$ for $M_Q = 0.5$ TeV and $M_1 = M_2 = 1$ TeV.

250 GeV is applied to each top c.f. figure 7. This study could be explored further using the top tagger of ref. [38], since, the transverse momentum of the top quarks peak around 300 GeV, i.e., the tops are boosted[13]. For $\tilde{h}_0$ masses in the multi-TeV range one could employ the top tagging methods of ref. [42].[14] Note that the two LW-states $\tilde{h}_0$ and $\tilde{p}_0$ are necessarily close to each other in case of a low SM-like Higgs mass by virtue of the tree-level relation (5.1). The effect of which can be seen in figure 7 where the individual parts are given. We have chosen $M_{\bar{t}t}$-bins of 5, 15 and 30 GeV respectively for $\sqrt{S} = 14$ TeV. A bin-size of 5 GeV seems unrealistic (in view of detector resolutions), whereas 15 GeV can be achieved and 30 GeV might very well be the reference value for early publications. A fundamental particle is described by its mass, spin and to some extent its interactions. So far we have not addressed the spin. The latter can be determined, as usual, through angular distributions. In [44], c.f. figure 15, the so-called Collins-Soper angle is advocated as promising observable.

We would like to add that the simulations were performed with LO order QCD backgrounds. For an assessment of NLO corrections we refer the reader to figure 2 in [44]. Besides the fact that they are not too large in the low mass region the important thing is that the shape is very similar to LO and thus very different to a resonant structure. In regard to the values of the $d\sigma(gg \to \bar{t}t)/dM_{\bar{t}t}$ differential cross section it should be kept in mind that it is not the top-pair that is observed in the detector. The efficiency of the top-reconstruction is estimated to be about 5% [55, 56]. The effects of the Higgs resonances for $\sqrt{S} = 7$ TeV seem to small to be observed and we have relegated the corresponding plot to appendix A.5 figure 14(right). In that case the gluon density is too small and $\bar{q}q \to g \to \bar{t}t$

[13] The search strategies outlined in refs. [39–41] can, also, be applied here as well.

[14] For a review of top tagging we refer the reader to ref. [43]

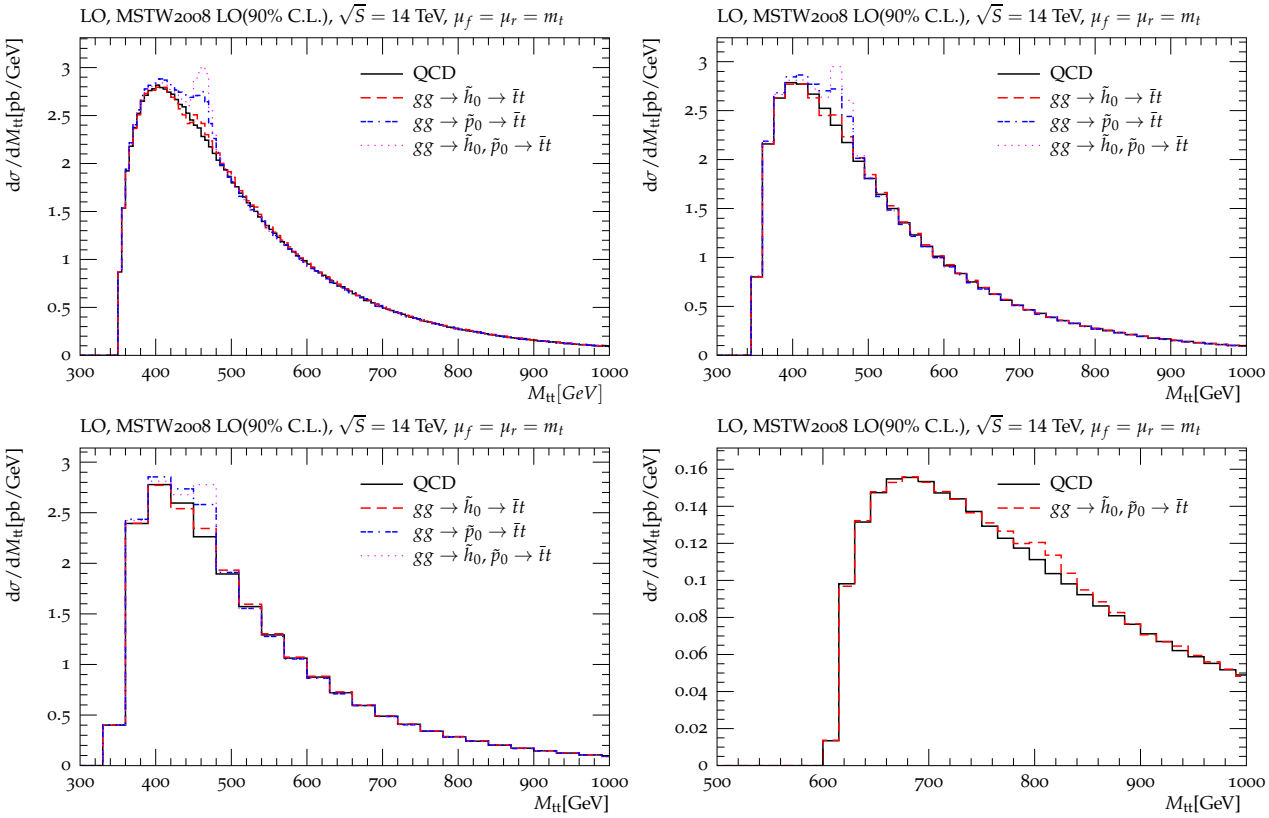

Figure 7. Histograms of the top pair invariant mass, $M_{\bar{t}t}$, for $gg \to \bar{t}t$ for $\sqrt{S} = 14\,\text{TeV}$. (top left)(top right) and (bottom left) for 5/15/30 GeV-bins, respectively. A dip-peak structure is to observed by the interference of the QCD-background with LW Higgs states. In these figures we have chosen the following mass values $m_{\tilde{h}_0} = 450$ GeV and $m_{\tilde{p}_0} = 467$ GeV which implies with eq. (5.1) $m_{h_0} = 125$ GeV. (bottom right) We plot M_{tt} for $m_{\tilde{h}_0} = 800$ GeV in 15 GeV bins where we assume $M_Q = M_u = M_d = 500$ GeV where the signal to background ratio is significantly improved by p_T-cut of 250 GeV to each top.

becomes more important. The latter being in a color octet representation, does not interfere with the LW contributions which is in a color singlet representation which leads to a reduction of the effect.

6 The $gg \to h_0 h_0 \to b\bar{b}\gamma\gamma$ channel at the LHC

In this section we will access the observability for double Higgs boson production in the LWSM [15] being the more promising than the $\tilde{p_0}h_0$-channel, for light Higgs boson masses in the range of $\sim 120 - 130$ GeV in the $gg \to h_0 h_0 \to \gamma\gamma b\bar{b}$ channel. This channel is of particular relevance, since, searches for the SM Higgs boson at ATLAS exclude SM Higgs boson masses at 95% C.L. in the range $155 - 190$ GeV and $295 - 450$ GeV [62] and at CMS

[15]The $h_0 h_0 \to \gamma\gamma b\bar{b}$ channel has been studied in the past in the context of the Randal–Sundrum model by both ATLAS [57] and CMS [58, 59], in the SM and MSSM [32, 60], and, most recently, in the context of a hidden sector Higgs boson [61].

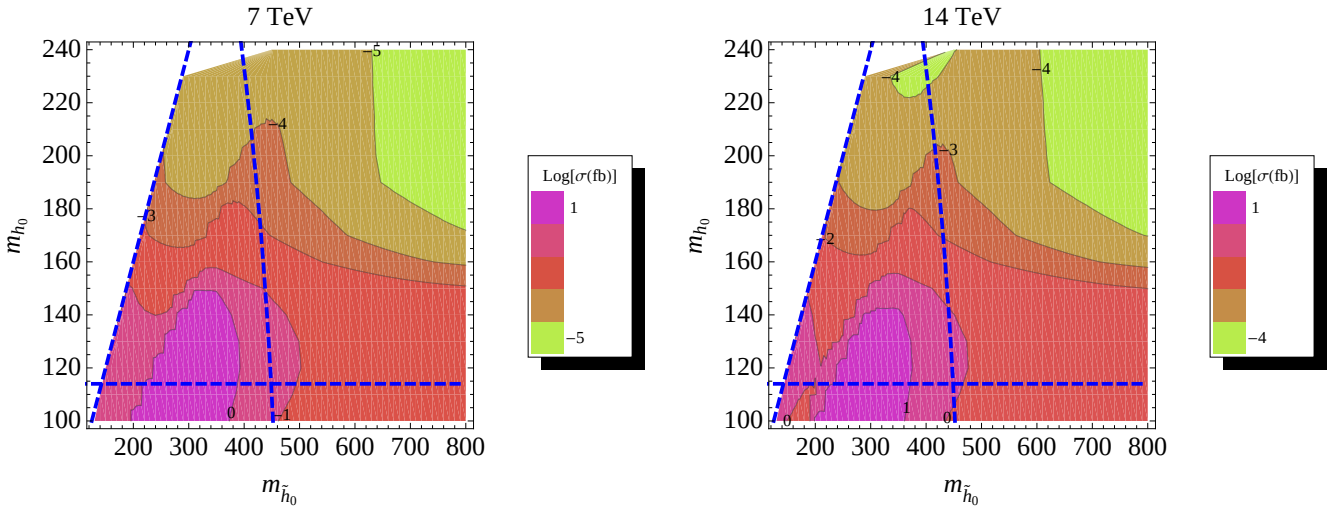

Figure 8. Contour plot of the total cross section (in fb) for $gg \to h_0 h_0 \to b\bar{b}\gamma\gamma$ ($\sqrt{S} = 7/14$ TeV respectively) versus the light Higgs boson mass, m_h and heavy Higgs boson mass, $m_{\tilde{h}}$ for $M_Q = 0.5$ TeV and $M_1 = M_2 = 1$ TeV.

exclude SM Higgs boson masses at 90% C.L. in the range $145 - 480$ GeV [63] [16]. This suggests the SM-like Higgs boson should reside in the low mass region, i.e, $m_{h_0} < 145$ GeV.

Shown in figure 8 are scans at both $\sqrt{S} = 7/14$ TeV respectively of the cross section $\sigma(h_0 h_0 \to \gamma\gamma b\bar{b})$ over the plane of $(m_{h_0}, m_{\tilde{h}_0})$. At $\sqrt{S} = 14$ TeV we choose three benchmark points listed in Table 1. At 7 TeV, $\sigma(h_0 h_0 \to \gamma\gamma b\bar{b})$ is less than or close to 1 fb throughout the plane of $(m_{h_0}, m_{\tilde{h}_0})$. This is before any sort of event selection which would reduce this by a factor of 10. Bearing in mind that the 7 TeV LHC is expected to accumulate about 10 fb^{-1} of integrated luminosity before its upgrade to 14 TeV we do not follow 7 TeV any further.

At the LHC the signal process $pp \to \tilde{h}_0 \to h_0 h_0 \to \gamma\gamma b\bar{b}$ will give rise to photons and jets of relatively high transverse momentum $p_T \sim 90$ GeV. In figure 9 we show the transverse momentum of the hardest photon and hardest jet to illustrate our point. Backgrounds consist of (i) di-photon plus multi-jets, (ii) single photon plus multi-jets, and (iii) multi-jet production. Our choice of photon isolation completely eliminates (iii) multi-jet production and (ii) single photon production from contention. Out of di-photon plus multi-jets, the dominant contributions are from the associated production of two photons and two heavy flavours, i.e., bottom and charm quarks. These are denoted as $\gamma\gamma QQ$ where $Q = c, b, \bar{b}, \bar{c}$. In addition, there are backgrounds from $\gamma\gamma Qj$ and $\gamma\gamma jj$ where $j = u, d, s, g$. Photons and jets from these backgrounds tend to be softer than those from the our signal process (see figure 9).

In our simulations we model b–tagging utilizing information in the event history of the Monte Carlo we are using. We label a jet a b–tag if a partonic b-quark of at least 5 GeV of transverse momentum is found in a cone of $R = 0.3$ around the axis of the jet. If no

[16] These bounds apply to the SM. For the LWSM we would expect, from the viewpoint of the HD-formalism, very similar or slightly stronger bounds.

b-quark is found, then we check in this order for a c-quark and τ-lepton. If no heavy quark or lepton is found, we label the jet a light jet. Depending on which label the jet receives we apply the following weights: $\epsilon_b(E_T, \eta)$, $\epsilon_{\text{mistag},c} = 10\%$, $\epsilon_{\text{mistag},\tau} = 5\%$, and $\epsilon_{\text{mistag},j} = 0.5\%$ [55, 64][17], which is reflected in the results in table 2.

For the computation of the backgrounds we have applied several parton–level cuts to regulate any soft or collinear divergences. We require two k_T-jets with $D = 0.7$ and

$$p_T^\gamma > 20 \text{ GeV} , \quad p_T^j > 20 \text{ GeV} , \tag{6.1}$$
$$|\eta^\gamma| < 2.5 , \quad |\eta^j| < 2.5 , \quad R_{\gamma j} > 0.3 , \quad R_{\gamma\gamma} > 0.3 .$$

For the signal process, $pp \to \tilde{h}_0 \to h_0 h_0 \to \gamma\gamma b\bar{b}$, we have not applied any parton–level cuts as there are no soft or collinear divergences.

We simulate events at the LHC using the Monte Carlo program `Sherpa 1.3.0` [65–68]. We have implemented the LWSM into `Sherpa` and have subsequently generated matrix elements for $pp \to \tilde{h}_0 \to h_0 h_0 \to \gamma\gamma b\bar{b}$ using `Amegic++` [69]. The matrix elements for the background processes have been generated using `Comix` [70]. All events generated include hadronization and shower effects. The parton shower is a Catani-Seymour subtraction based shower which is performed by module `CSSHOWER++`. Hadronization is performed by the module `AHADIC++`. Additionally, the effects of soft QED radiation off hadron and tau decays has been simulated using the module `PHOTONS++`.

In order to analyze events we have written an analysis plugin for `Rivet 1.3.0` [71]. `Fastjet 2.4.2` has been used to perform the clustering of final state particles into jets [72]. We have implemented the following selection criteria in our analysis:

Cut 1:
- *Photon isolation:* i) $p_T > 20$ GeV ii) pseudo-rapidity range of $-2.5 < \eta_\gamma < 2.5$ are isolated photons if iii) $\sum_{R \geq R_{\gamma k}} E_T(k) < 0.1 p_T^\gamma$ is satisfied where $R_{\gamma k} \equiv \sqrt{(\phi_\gamma - \phi_k)^2 + (\eta_\gamma - \eta_k)^2}$ and $R = 0.3$. Here k can be at the particle-level either hadrons or photons with $|\eta_\gamma| > 2.5$ or $p_T^\gamma < 20$ GeV.
- Exactly two isolated photons are required.
- The hardest isolated photon is required to have a minimal transverse momentum of 40 GeV and $R_{\gamma\gamma} > 0.3$.

Cut 2: Exactly two k_T-jets with $D = 0.7$ in the pseudo-rapidity range of $-2.5 < \eta_j < 2.5$ with minimal transverse momentum, 30 GeV, are required.

Cut 3: At least one b–tagged jet.

Cut 4: The di–photon invariant mass $M_{\gamma\gamma}$ is required to be in the mass window, $|M_{\gamma\gamma} - m_{h_0}| \leq 2$ GeV.

Cut 5: The dijet invariant mass M_{bj} is required to be in the mass window, $|M_{bj} - m_{h_0}| \leq 20$ GeV.

[17] The expression for $\epsilon_b(E_T, \eta)$ is equal to the product of functions b_{E_T} and b_η. These functions are explicitly shown in ref. [64].

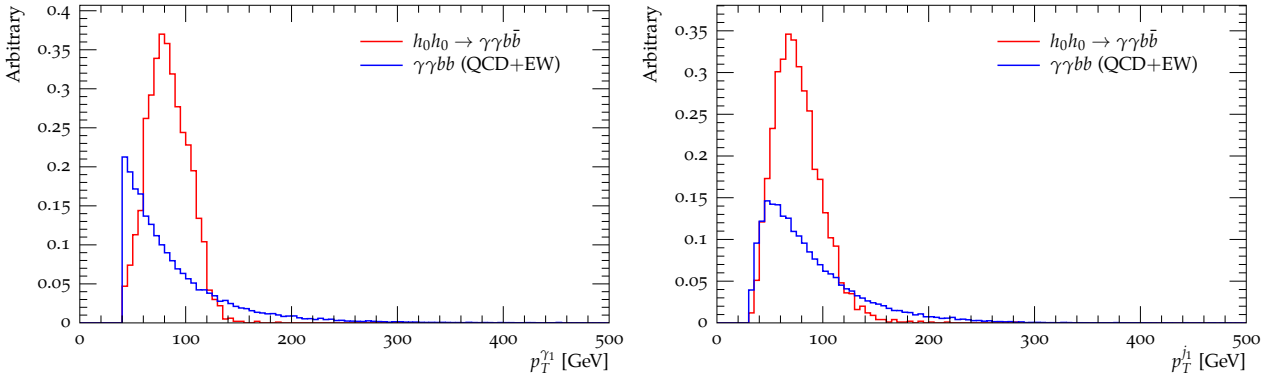

Figure 9. Shown (in arbitrary units) are the distributions for the signal process $h_0h_0 \to \gamma\gamma b\bar{b}$ (red) and one of the backgrounds, $\gamma\gamma bb$ (blue), in transverse momentum of the hardest jet $p_T^{j_1}$ (left) and hardest photon $p_T^{\gamma_1}$ (right).

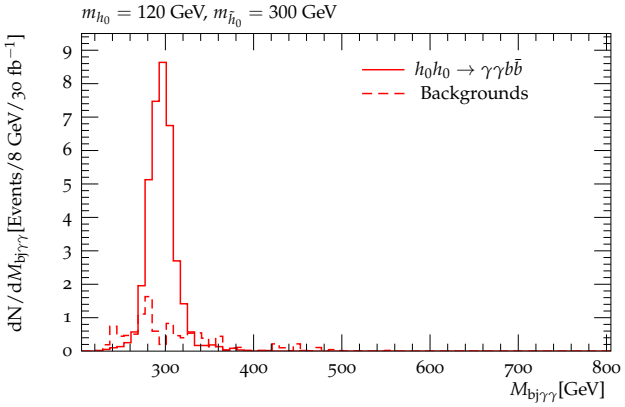

Figure 10. Shown is the distribution in the invariant mass of two jets and two photons, $M_{bj\gamma\gamma}$, in 8 GeV bins for 30 fb^{-1} of integrated luminosity at the $\sqrt{S} = 14$ TeV LHC.

Benchmark	m_{h_0}(GeV)	$m_{\tilde{h}_0}$(GeV)	$\delta m_{\tilde{h}_0}$(GeV)
(a)	120	300	40
(b)	130	445	45
(c)	130	550	50

Table 1. Shown in this table are the light Higgs boson mass parameters m_h, the LW Higgs boson mass parameters, $m_{\tilde{h}}$, and the mass window parameters $\delta m_{\tilde{h}_0}$ for benchmark points (a),(b), and (c).

Cut 6: The invariant mass $M_{bj\gamma\gamma}$ is required to be in the mass window, $|M_{bj\gamma\gamma} - m_{\tilde{h}_0}| \leq \delta m_{\tilde{h}_0}$. Values of our choice of $\delta m_{\tilde{h}_0}$ for each benchmark point are shown in Table 1.

Table 2 displays the efficiencies and cross sections for the backgrounds before and after selection cuts have been applied. Efficiencies and cross sections for the *signal process* are shown in Table 3. In figure 10 we show for 30 fb^{-1} of integrated luminosity in 8 GeV

	QCD+EW:	$\gamma\gamma jj$	$\gamma\gamma bb$	$\gamma\gamma cc$	$\gamma\gamma bc$	$\gamma\gamma bj$	$\gamma\gamma cj$
	$\sigma_{\rm gen}$(pb)	23.2	0.176	1.56	0.0840	0.519	6.26
	cut 1	0.390	0.370	0.306	0.295	0.344	0.354
	cut 2	0.363	0.358	0.386	0.435	0.406	0.366
	cut 3	0.0526	0.795	0.116	0.516	0.460	0.0920
	cut 4a	0.0212	0.0233	0.0247	0.0217	0.0240	0.0200
	cut 5a	0.249	0.229	0.232	0.242	0.264	0.203
	cut 6a	0.604	0.547	0.713	0.534	0.471	0.627
	$\epsilon_{\rm tot}$	2.37×10^{-5}	3.07×10^{-4}	5.60×10^{-5}	1.85×10^{-4}	1.93×10^{-4}	3.03×10^{-5}
(a)	$\sigma_{\rm eff}$(fb)	0.550	0.0527	0.0873	0.0156	0.100	0.190
	cut 4b	0.0150	0.0202	0.0139	0.0167	0.0221	0.0191
	cut 5b	0.221	0.213	0.174	0.242	0.234	0.276
	cut 6b	0.136	0.0567	0.129	0.138	0.165	0.130
	$\epsilon_{\rm tot}$	3.37×10^{-6}	2.56×10^{-5}	6.14×10^{-6}	3.67×10^{-5}	5.46×10^{-5}	8.06×10^{-6}
(b)	$\sigma_{\rm eff}$(fb)	0.0782	0.00431	0.00959	0.00309	0.0283	0.0505
	cut 4c	0.0150	0.0213	0.0199	0.0167	0.0221	0.0191
	cut 5c	0.221	0.213	0.174	0.242	0.234	0.274
	cut 6c	0.00723	0.0337	0.00289	0.0164	0.0303.	0.0.0122
	$\epsilon_{\rm tot}$	1.79×10^{-7}	1.52×10^{-5}	1.38×10^{-8}	4.36×10^{-6}	1.00×10^{-5}	7.58×10^{-7}
(c)	$\sigma_{\rm eff}$(fb)	0.00414	0.00261	2.15×10^{-5}	0.000366	0.00521	0.00475

Table 2. Table of cross sections (in pb) for benchmarks (a),(b), and (c) before selection cuts ($\sigma_{\rm gen}$) and with selection cuts ($\sigma_{\rm eff}$) for the backgrounds $QQ\gamma\gamma$, $Qj\gamma\gamma$, and $jj\gamma\gamma$ where $Q = c, b, \bar{c}, \bar{b}$ and $j = u, \bar{u}, d, \bar{d}, s, \bar{s}, g$ for $\sqrt{S} = 14$ TeV. Efficiencies (cuts 1–6) are relative where ϵ_{tot} is the cumulative efficiency. Cuts 1-3 are reproduced only once as they are the same for all three benchmarks.

$pp \to h_0 h_0 \to \gamma\gamma b\bar{b}$	(a)	(b)	(c)
$\sigma_{\rm gen}$(fb)	11.2	0.964	0.195
cut 1	0.594	0.675	0.693
cut 2	0.414	0.405	0.391
cut 3	0.734	0.760	0.748
cut 4	0.999	0.999	0.999
cut 5	0.601	0.567	0.586
cut 6	0.966	0.823	0.725
$\epsilon_{\rm tot}$	0.105	0.097	0.0861
$\sigma_{\rm eff}$(fb)	1.18	0.0935	0.0168

Table 3. Cross sections (in fb) before selection and after selection for benchmarks (a) $m_{h_0} = 120$ GeV, $m_{\tilde{h}_0} = 300$ GeV, (b) $m_{h_0} = 130$ GeV, $m_{\tilde{h}_0} = 445$ GeV, and (c) $m_{h_0} = 130$ GeV, $m_{\tilde{h}_0} = 550$ GeV. Efficiencies (cuts 1-6) are relative where $\epsilon_{\rm tot}$ is the cumulative efficiency.

$pp \to h_0 Z \to \gamma\gamma b\bar{b}$	(a) $m_{h_0} = 120$ GeV, $m_{\tilde{h}_0} = 300$ GeV
σ_{gen}(fb)	32.3
cut 1	0.745
cut 2	0.489
cut 3	0.772
cut 4	0.999
cut 5	0.184
cut 6	0.422
ϵ_{tot}	0.0218
σ_{eff}(fb)	0.703

Table 4. Cross sections (in fb) for $h_0 Z \to \gamma\gamma b\bar{b}$ before selection and after selection for benchmark (a) $m_{h_0} = 120$ GeV, $m_{\tilde{h}_0} = 300$ GeV. Efficiencies (cuts 1-6) are relative where ϵ_{tot} is the cumulative efficiency.

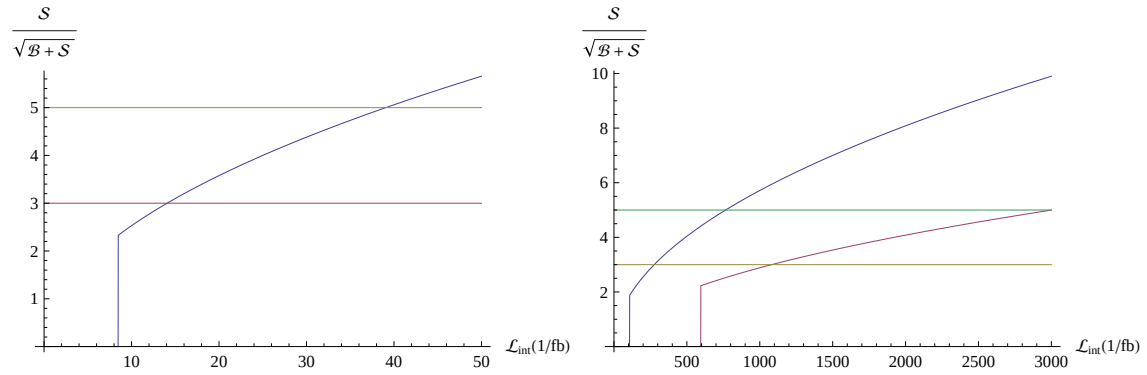

Figure 11. Shown is the significance $\mathcal{S}/\sqrt{\mathcal{B}+\mathcal{S}}$ plotted against luminosity for benchmarks (a) (left) and benchmarks (b) in blue and (c) in red (right). The upper and lower horizontal lines mark observation significances of 3σ and 5σ. The vertical lines represent 10 events.

bins the invariant mass of the $bj\gamma\gamma$ system for the signal scenario (a) and the sum of all backgrounds before cut 6 has been applied. For benchmark (a) we can expect to establish a 5σ-discovery with as little as 20 fb^{-1}. For benchmarks (b) and (c) outlook is not so optimistic. For scenario (b) we expect to reach 5σ at 700 fb^{-1} and for scenario (c) we would need 3000 fb^{-1} of integrated luminosity. The primary reason for the reduced cross sections for scenarios (b) and (c) is that the dominant decay mode for the heavy LW Higgs $\tilde{h}_0$ is $\tilde{h}_0 \to \bar{t}t$ with $\text{Br}_{\tilde{h}_0} \sim 95\%$.

To this end we would like to mention that for benchmark (a) there is a background from Zh_0 production[18]. Efficiencies and cross sections are shown in table 4. It is worth mentioning that our analysis can be adapted for this case be changing our mass reconstruction hypothesis slightly. Instead of requiring the invariant mass M_{bj} to be in mass window around the h_0, we would instead, stipulate that in be in a mass window around

[18]Note that benchmarks (b) and (c) this channel is dominated by top pairs.

the Z boson. Additionally, the invariant mass $M_{\gamma\gamma bj}$ should reconstruct the $\tilde{p}_0$.

7 Conclusions

In this paper we have investigated the possibility of a light LW Higgs sector. As mentioned in the introduction SM-like Higgs sectors, such as the one of the LWSM, are not yet very well constrained as the the Higgs enters one-loop correction only logarithmically for larger masses and couples only very weakly to leptons obscuring the clean di-lepton detection channel. In practice this means that although the LW gauge bosons and the LW fermions are constrained to lay in the few-TeV range the Higgs sector could be very low. In view of indirect (EWPO) and direct (collider) constraints we have assumed the SM-like Higgs boson to be below then 150 GeV-value.

We have investigated such a possibility by looking at the cross sections $gg \to h_0 h_0$ and $gg \to \tilde{p}_0 h_0$ c.f. figures 4,6 and the spectrum of $gg \to \bar{t}t$ figure 7. Whereas the $gg \to h_0 h_0$ channel is outside reach at the LHC in the SM, it is enhanced in the LWSM in the case where the LW-like Higgs is twice as heavy as the SM-like Higgs ($m_{\tilde{h}_0} > 2m_{h_0}$) and can decay at resonance through $gg \to \tilde{h}_0 \to h_0 h_0$ shown in figure 1(a). The pseudoscalar $gg \to \tilde{p}_0 \to \tilde{p}_0 h_0$ subprocess is close but not at resonance and turns out to be large as compared to SM Higgs channel but much smaller than the case discussed above as can be inferred from figure 6 vs 4. In our signal analysis we have therefore focused on the latter through $gg \to h_0 h_0 \to \bar{b}b\gamma\gamma$ and from table 3 we see that the benchmark points (a) to (c) $(m_{h_0}, m_{\tilde{h}_0}) = \{(120, 300), (130, 445), (130, 550)\}$ GeV reach 10 events for integrated luminosities of $\{8.5, 107, 595\}\,\text{fb}^{-1}$ and the 5σ-discovery for $\{20, 700, 3000\}\,\text{fb}^{-1}$ as can be seen from figure 11. In regard to these numbers we would like to add that the LHC is expected to collect $335\,\text{fb}^{-1}$ at 14 TeV from 2012 to 2020 before the upgrade to the Super LHC where $1500\,\text{fb}^{-1}$ is the reference number for 2025.

The Higgs pair production cross section decreases rapidly for a $\tilde{h}_0$ with a mass above the top pair production threshold of $2m_t$. In this region the intermediate states $\tilde{h}_0$ and $\tilde{p}_0$ decay mostly into top pairs as this is the dominant decay mode, c.f. figure 15(right). In light of this it seems natural to investigate top pair production within the LWSM. It is found though that the dip-peak or in general the visibility of the resonance is diluted when the width is large which happens when the intermediate states can decay into top pairs c.f. figure 7. In the latter case the signal to background ratio can be significantly improved by applying p_T-cut of 250 GeV is applied to each top quark. An example is given in figure 7(bottom-right) for $m_{h_0}, m_{\tilde{h}_0} = (125, 800)$ GeV. Further suggestions on how to improve the signal are given in section 6.

Moreover, in this work we have also clarified a few things in the LWSM itself such as the tree-level sum rules in appendix C.1, how to reduce hyperbolic diagonalizations to standard methods in appendix C and the issue of spurious versus CP-violating phases in the LW generation Yukawa matrix in appendix C.2. Moreover we have computed box diagrams with two vector (gluon) and pseudo/scalar (Higgs) flavour-changing vertex analytically,

extending the results from the SM [37] and MSSM [33].[19] The results are presented in appendix A.2.

Acknowledgments

We are grateful to Alexander Belyaev, Thomas Rizzo, Tilman Plehn, Gustaaf Brooijmans, Rikkert Frederix, and Francesco Sannino for discussions. RZ gratefully acknowledges the support of an advanced STFC fellowship. TF would like to thank the CERN Theory Division for their support.

A Results and definitions for $gg \to h_0 h_0 / h_0 \tilde{p}_0$ process

In this appendix all masses correspond to the physical masses and for the sake of notational simplicity we shall use the notation:

$$m_{x,\text{phys}} \to m_x \tag{A.1}$$

for all the masses. We shall retain the subscript phys for the Yukawa matrices.

A.1 Triangle graph

The triangle graph in the SM is given by[20]:

$$\mathcal{A}_0^{\triangle}|_{\text{SM}}(gg \to h_0 h_0) = \frac{-3m_H^2 s}{s - m_H^2 + i m_H \Gamma_H} F_{1/2}(\beta_q) \ , \quad \beta_x = 4m_{x,\text{phys}}^2/s \tag{A.2}$$

where

$$F_{1/2}(x) = -2x(1 + (1-x)f(x)) \tag{A.3}$$

and

$$f(x) = \begin{cases} \text{Arcsin}^2(1/\sqrt{x}) & x \geq 1 \\ -\frac{1}{4}(\ln\left(\frac{1+\sqrt{1-x}}{1-\sqrt{1-x}}\right) - i\pi)^2 & x < 1 \end{cases} . \tag{A.4}$$

c.f. [33] for example[21]

A.1.1 $gg \to h_0/\tilde{h}_0 \to h_0 h_0$ triangles

Since the Higgs sector (2.14) does not contribute to the loop, the LW-contribution can be obtained from the SM with modification of the vertices and taking into account mixing factors. The coupling of the Higgs to the triangle itself is modified by mixing factors in eq. (2.8) $s_{H-\tilde{H}}$ and $\tilde{s}_{H-\tilde{H}} = -s_{H-\tilde{H}}$ for the standard and the LW Higgs boson respectively. The triple Higgs boson vertices h_0^3 and $\tilde{h}_0 h_0^2$ are modified in the same way multiplying in

[19] Flavour-changing vertices were computed in the MSSM in the squark sector [73] whereas here the top fermions are considered.

[20] This notation agrees with [37] as follows: $a_{0,2}^{\triangle} = \text{gauge1(2)(triangle)}$.

[21] The function $f(x)$ relates to the Passarino-Veltman function as follows: $2m_x^2/s\Big(2 + (4m_x^2 - s)C_0(0, s, 0, m_x^2, m_x^2, m_x^2)\Big) = \beta_x(1 + (1-\beta_x)f(\beta_x))$.

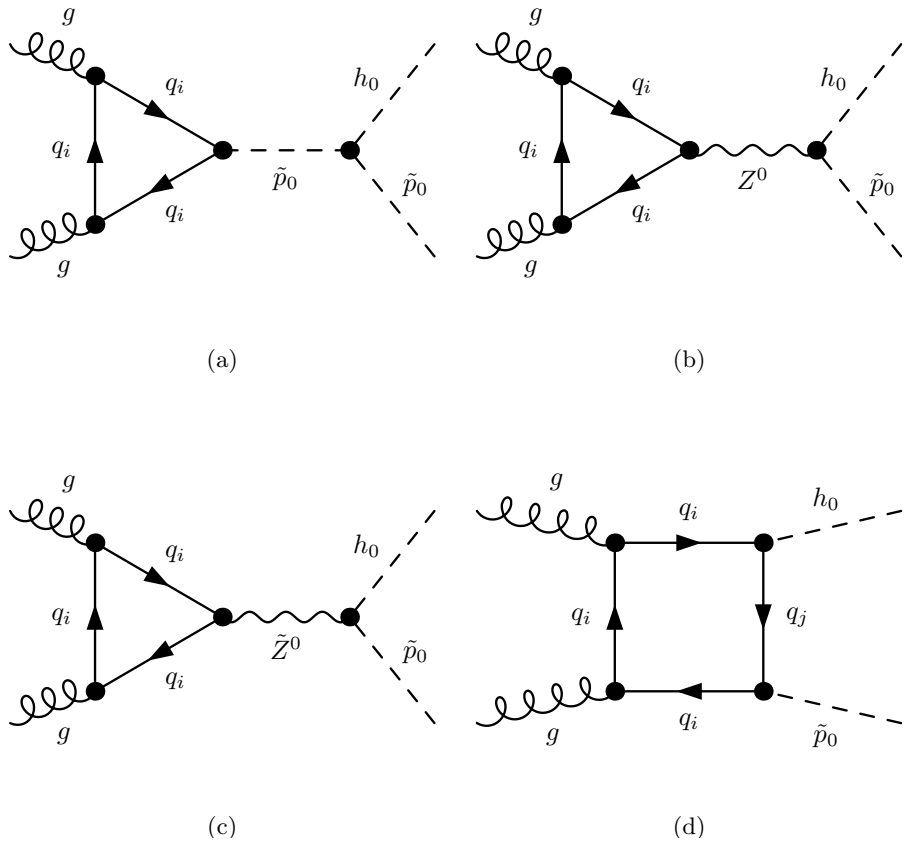

Figure 12. (a–c) Triangle graphs for $q = (t, \tilde{t}, \tilde{T}, b, \tilde{b}, \tilde{B})$ and (d) one out of six box graphs for $q_i, q_j = (t, \tilde{t}, \tilde{T}, b, \tilde{b}, \tilde{B})$.

addition a factor of $s^2_{H\text{–}\tilde{H}}$. Furthermore $\lambda v^2 = 2m^2_{h_0,\text{phys}}/(1 + r^2_{h_0})$, exceptionally insisting on the subscript phys, according to eq. (2.7) which leads to:

$$\mathcal{A}_0^{\triangle}(gg \to h_0 h_0) = \frac{-3s^4_{H\text{–}\tilde{H}} m^2_{h_0}}{1 + r^2_{h_0}} \Big(\frac{1}{s - m^2_{h_0} + i m_{h_0}\Gamma_{h_0}} - \frac{1}{s - m^2_{\tilde{h}_0} - i m_{\tilde{h}_0}\Gamma_{\tilde{h}_0}} \Big) s\ \tilde{F}_{1/2} \quad \text{(A.5)}$$

with

$$\tilde{F}_{1/2} = \frac{(g_{t,\text{phys}})_{11}}{m_t} F_{1/2}(\beta_t) - \frac{(g_{t,\text{phys}})_{22}}{m_{\tilde{t}}} F_{1/2}(\beta_{\tilde{t}}) - \frac{(g_{t,\text{phys}})_{33}}{m_{\tilde{t}'}} F_{1/2}(\beta_{\tilde{t}'})\,. \quad \text{(A.6)}$$

The process $gg \to h_0\tilde{p}_0$ consist of triangles and boxes shown figure 12. The triangle contributions can be broken down into contributions originating from:

1. s–channel $\tilde{p}_0$ exchange shown in figure 12(a),
2. s–channel Z_0 exchange shown in figure 12(b), and
3. s–channel $\tilde{Z}_0$ exchange shown in figure 12(c).

We denote the contribution of all triangle diagrams by

$$\mathcal{A}_0^{\triangle}(gg \to h_0\tilde{p}_0) = \mathcal{A}_0^{\triangle,\tilde{p}_0} + \mathcal{A}_0^{\triangle,Zt} + \mathcal{A}_0^{\triangle,Zb}\,, \quad \text{(A.7)}$$

where the amplitudes are further defined in the next subsection.

A.1.2 $gg \to \tilde{p}_0 \to h_0\tilde{p}_0$ triangles

$$\mathcal{A}_0^{\triangle,\tilde{p}_0}(gg \to \tilde{p}_0 h_0) = i\frac{s_{H-\tilde{H}}}{1+r_{h_0}^2}\left(\frac{2m_{h_0}^2}{s-m_{\tilde{p}_0}^2}s\ \tilde{P}_{1/2}\right) \tag{A.8}$$

where for $\tilde{P}_{1/2} = \tilde{F}_{1/2}(F_{1/2}(\beta_x) \to P_{1/2}(\beta_x))$ with $P_{1/2}(\beta_x) = \beta_x f(\beta_x)$ in accordance with [33].

A.1.3 $gg \to Z_0/\tilde{Z}_0 \to h_0\tilde{p}_0$ triangles

$$\mathcal{A}_0^{\triangle,Zq} = i\frac{ev^2 s_{\tilde{H}}(\cosh\theta_Z + \sinh\theta_Z)}{\cos\theta_W \sin\theta_W}(m_{\tilde{p}_0}^2 - m_{h_0}^2) \times \tag{A.9}$$
$$\sum_{j=1}^{3}\eta_{jj}\left(\frac{(g_{R,\text{phys}}^{Zq_j\bar{q}_j} - g_{L,\text{phys}}^{Zq_j\bar{q}_j})(1-\frac{s}{m_Z^2})}{s-m_Z^2+im_Z\Gamma_Z} - \frac{(g_{R,\text{phys}}^{\tilde{Z}q_j\bar{q}_j} - g_{L,\text{phys}}^{\tilde{Z}q_j\bar{q}_j})(1-\frac{s}{m_{\tilde{Z}}^2})}{s-m_{\tilde{Z}}^2-im_{\tilde{Z}}\Gamma_{\tilde{Z}}}\right)(1-\beta_{q_j}f(\beta_{q_j}))$$

where the function f is defined in (A.4) and $s_{\tilde{H}} \equiv \sinh(\phi_h)$ in accord with our notation in eq. (2.8). Note this is due to the fact that prior to diagonalization only the $\tilde{h}_0\tilde{p}_0 Z$-coupling but not the $h_0\tilde{p}_0 Z$-coupling is present. The couplings of quarks to gauges bosons are parametrized as follows:

$$\mathcal{L} = \sum_{f=t,b}\left(\bar{\Psi}_L^f g_L^{Zf\bar{f}}(\not{Z}+\not{\tilde{Z}})\Psi_L^f + \bar{\Psi}_R^f g_R^{Zf\bar{f}}(\not{Z}+\not{\tilde{Z}})\Psi_R^f\right)_{\text{phys}} \tag{A.10}$$

The superscript "phys" indicates that all fields and couplings are understood to the physical ones. The physical couplings $g_{R,\text{phys}}^{Zf\bar{f}}$ are obtained from the expressions in Eqs. (A.11) to (A.14) as

$$g_{L,\text{phys}}^X = S_L^\dagger g_L^X S_L\ , \qquad g_{R,\text{phys}}^X = S_R^\dagger g_R^X S_R\ ,,$$

where X stands for $Zt\bar{t}$ or $Zb\bar{b}$ respectively.

$$g_R^{Zt\bar{t}} = -\frac{e(\cosh\theta_Z+\sinh\theta_Z)}{6c_w s_w}\begin{pmatrix}-4(1-c_w^2) & 0 & 0\\ 0 & 4(1-c_w^2) & 0\\ 0 & 0 & -4c_w^2+1\end{pmatrix} \tag{A.11}$$

$$g_L^{Zt\bar{t}} = -\frac{e(\cosh\theta_Z+\sinh\theta_Z)}{6c_w s_w}\begin{pmatrix}4c_w^2-1 & 0 & 0\\ 0 & 4(1-c_w^2) & 0\\ 0 & 0 & -4c_w^2+1\end{pmatrix} \tag{A.12}$$

$$g_R^{Zb\bar{b}} = -\frac{e(\cosh\theta_Z+\sinh\theta_Z)}{6c_w s_w}\begin{pmatrix}2(1-c_w^2) & 0 & 0\\ 0 & -2(1-c_w^2) & 0\\ 0 & 0 & 2c_w^2+1\end{pmatrix} \tag{A.13}$$

$$g_L^{Zb\bar{b}} = -\frac{e(\cosh\theta_Z+\sinh\theta_Z)}{6c_w s_w}\begin{pmatrix}-2c_w^2-1 & 0 & 0\\ 0 & -2(1-c_w^2) & 0\\ 0 & 0 & 2c_w^2+1\end{pmatrix} \tag{A.14}$$

A.2 Boxes for $gg \to h_0 h_0$ and $gg \to h_0 \tilde{p}_0$

For definiteness we shall give one graph, the one indicated in figure 1(right):

$$\Big[(a_0)^{\square}_{15})(m_i,m_j)(\tilde{P}_0)_{\mu\nu} + ((a_2)^{\square}_{15})(m_i,m_j)(\tilde{P}_2)_{\mu\nu}\Big]|_{\text{figure 1(right)}} + X_{\mu\nu} =$$
$$(4\pi^2 i)\int \frac{d^4l}{(2\pi)^4}\mathrm{tr}[\gamma_\mu S_{m_i}(l+p_1)\gamma_\nu S_{m_i}(l+p_1+p_2)\mathbf{1}S_{m_j}(l+p_1+p_2+p_3)\gamma_5 S_{m_i}(l)]\ ,$$

for vertices $\mathbf{1}$ and γ_5. The term $X_{\mu\nu}$ stands for are structures vanishing when contracted with the according polarization vectors. As stated in the main text in this notation only $(a_{0,2})^{\square}_{11}$ do contribute in the SM, since there are no fundamental pseudoscalars, and are related to the results in [37] as: $(a_{0,2})^{\square}_{11} = \text{gauge1(2)}(box)$.

In the following we shall present our results for the box graphs. The analytic computations have been performed with the aid of FeynCalc [74]. We are not aware of them being published elsewhere for the case where the flavour can change between the Higgs vertices. The gluon momenta are p_1 and p_2 whereas the Higgs pair momenta are p_3 and are p_4. We use the convention where all momenta are incoming, i.e. $p_1 + p_2 = -p_3 - p_4$. The result is given in terms of the Mandelstam variables

$$s = (p_1+p_2)^2\ , \quad t = (p_1+p_3)^2\ , \quad u = (p_1+p_4)^2 \tag{A.15}$$

and further shorthands

$$T_i = t - m_i^2\ , \quad U_i = u - m_i^2 \tag{A.16}$$

for $i = 3, 4$.

$$\begin{aligned}
&(a_0)^{\square}_{11}(m,M)\\
&= \frac{1}{s}\Big\{4s + 8M^2 s C_{12} + 2s((m+M)(2M^2(m+M) - Ms) - M^2(t+u))(D_{123}+D_{132}+D_{213})\\
&+ (m_3^2 + m_4^2 - 2(m+M)^2)\big[T_3C_{13} + T_4C_{24} + U_3C_{23} + U_4C_{14} - (tu - m_3^2m_4^2 + s(m^2-M^2))D_{132}\big]\\
&+ \{m \leftrightarrow M\}\Big\}
\end{aligned}$$

$$\begin{aligned}
&(a_0)^{\square}_{51}(m,M)\\
&= \frac{(-i)}{s}\Big\{ - 2s(mMs + M^2(m_3^2 - m_4^2))(D_{123}+D_{132}+D_{213})\\
&+ (m_3^2 - m_4^3)\big[T_3C_{13} + T_4C_{24} + U_3C_{23} + U_4C_{14} - (tu - m_3^2m_4^2 + s(m^2-M^2))D_{132}\big]\\
&+ \{m \leftrightarrow M\}\Big\}
\end{aligned}$$

$$(a_0)^{\square}_{55}(m,M) = -(a_0)^{\square}_{11}(m,-M) = -(a_0)^{\square}_{11}(-m,M)$$

$$\begin{aligned}
&(a_2)^{\square}_{11}(m,M) \\
&= \frac{1}{tu-m_3^2m_4^2}\Big\{(t^2+u^2-(4m^2+4mM)(t+u)+4(m-M)(m+M)^3+2m_3^2m_4^2)sC_{12} \\
&+ (m_3^2m_4^2+t^2-2t(m+M)^2)(T_3C_{13}+T_4C_{24}-stD_{213}) \\
&+ (m_3^2m_4^2+u^2-2u(m+M)^2)(U_3C_{23}+U_4C_{14}-suD_{123}) \\
&- (t^2+u^2-2m_3^2m_4^2)(t+u-2(m+M)^2)C_{34} \\
&- (t+u-2(m+M)^2)((tu-m_3^2m_4^2)(m^2+M^2)+s(m^2-M^2)^2)(D_{123}+D_{132}+D_{213})\Big\} \\
&+ (M^2-m^2)(2(m+M)^2(u(2s+t)-m_3^2m_4^2)-m_3^2m_4^2(s-t-u)-tu(m_3^2+m_4^2)-2su^2)sD_{123} \\
&+ (M^2-m^2)(2(m+M)^2(t(2s+u)-m_3^2m_4^2)-m_3^2m_4^2(s-t-u)-tu(m_3^2+m_4^2)-2st^2)sD_{213} \\
&+ \{m\leftrightarrow M\}
\end{aligned}$$

$$\begin{aligned}
&(a_2)^{\square}_{51}(m,M) \\
&= \frac{-i}{tu-m_3^2m_4^2}\Big\{(2(M^2-m^2)(u-t)-t^2+u^2)sC_{12} \\
&+ (m_3^2m_4^2-t^2)(T_3C_{13}+T_4C_{24}-stD_{213}) \\
&+ (m_3^2m_4^2-u^2)(U_3C_{23}+U_4C_{14}-suD_{123}) \\
&+ ((t+u)^2-4m_3^2m_4^2)(t-u)C_{34} \\
&+ (t-u)((tu-m_3^2m_4^2)(m^2+M^2)+s(m^2-M^2)^2)(D_{123}+D_{132}+D_{213})\Big\} \\
&+i\ (M^2-m^2)((s-t+u)(tu-m_3^2m_4^2)+2su(u-t)))sD_{123} \\
&-i\ (M^2-m^2)((s-u+t)(tu-m_3^2m_4^2)+2st(t-u)))sD_{213} \\
&+ \{m\leftrightarrow M\}
\end{aligned}$$

$$(a_2)^{\square}_{55}(m,M) = -(a_2)^{\square}_{11}(m,-M) = -(a_2)^{\square}_{11}(-m,M) \tag{A.17}$$

We would like to add three comment concerning symmetries in the amplitudes. First the relation,

$$(a_{0,2})^{\square}_{55}(m,M) = -(a_{0,2})^{\square}_{11}(m,-M) = -(a_{0,2})^{\square}_{11}(-m,M) \tag{A.18}$$

follows from commuting the γ_5 from one pseudoscalar vertex to the other one. It is easy to see that doing this is equivalent to an overall factor of -1 and changing all the masses in the nominators where the γ_5 passed from say $M \to -M$. This in turn is equivalent to eq. (A.18). Second, the amplitudes $(a_{0,2})^{\square}_{15}(m,M)$ can be obtained from $(a_{0,2})^{\square}_{51}(m,M)$ by interchanging p_3 and p_4 which results in:

$$p_3 \leftrightarrow p_4 \quad \Rightarrow \quad m_3 \leftrightarrow m_4\ , u \leftrightarrow t\ , C_{13} \leftrightarrow C_{14}\ , C_{23} \leftrightarrow C_{24}\ , D_{123} \leftrightarrow D_{213} \tag{A.19}$$

Thirdly the $a^{\square}$ are manifestly symmetric under interchange of t and u. We note that the matrix element without polzarization vectors contracted is symmetric under interchange

$(p_1,\mu) \leftrightarrow (p_2,\nu)$ which results in $t \leftrightarrow u$. Thus $(a)^{\square}P_{\mu\nu}$ is symmetric and since P_0, P_2, $\tilde{P}_0$ ($\tilde{P}_2$) are even (odd) respectively the same property holds for $(a_0)^{\square}_{(15/51)}$, $(a_{0,2})^{\square}_{(11/55)}$ ($(a_2)^{\square}_{(15/51)}$) as can be seen from the formulae above.

A.3 Tensor structures

The tensor structure for the parity-even case P_0, P_2 are given in [37]:

$$\begin{aligned} S_z = 0: \qquad & P_0^{\mu\nu} = g^{\mu\nu} - \frac{p_1^\nu p_2^\mu}{(p_1p_2)} \\ S_z = 2: \qquad & P_2^{\mu\nu} = g^{\mu\nu} + \frac{p_3^2 p_1^\nu p_2^\mu}{p_T^2(p_1p_2)} - \frac{2(p_2p_3)p_1^\nu p_3^\mu}{p_T^2(p_1p_2)} - \frac{2(p_1p_3)p_2^\mu p_3^\nu}{p_T^2(p_1p_2)} + \frac{2p_3^\mu p_3^\nu}{p_T^2}\,, \end{aligned}$$

whereas the one for the parity-odd case [33] are:

$$\begin{aligned} S_z = 0: \qquad & \tilde{P}_0^{\mu\nu} = \frac{1}{(p_1p_2)}\epsilon^{\mu\nu p_1 p_2} \\ S_z = 2: \qquad & \tilde{P}_2^{\mu\nu} = \frac{p_3^\mu \epsilon^{\nu p_1 p_2 p_3} + p_3^\nu \epsilon^{\mu p_1 p_2 p_3} + (p_2p_3)\epsilon^{\mu\nu p_1 p_3} + (p_1p_3)\epsilon^{\mu\nu p_2 p_3}}{(p_1p_2)p_T^2}\,, \end{aligned}$$

where $p_T^2 = 2(p_1p_3)(p_2p_3)/(p_1p_2) - p_3^2$ and the projectors $\{P_0, \tilde{P}_0, P_2, \tilde{P}_2\}$ are normalized as follows:

$$P_i \in \{P_0, \tilde{P}_0, P_2, \tilde{P}_2\} \quad \text{s.t.} \quad P_iP_j = 2\delta_{ij}\,. \tag{A.20}$$

Note that there are two more structures with the properties of $\tilde{P}_0$ and on more with the property of $\tilde{P}_2$. This is of no relevance as we have performed the computation by contracting with helicity vectors. The basis that we have chosen is $p_1 = (p,0,0,p)$, $p_2 = (p,0,0,-p)$, $\epsilon(p_1,\pm) = \epsilon(p_2,\mp) = 1/\sqrt{2}(0,-1,\mp i,0)$ $p_3 = (\sqrt{m_3^2+q^2},0,q\sin(\theta),q\cos(\theta))$ and $p_4 = (\sqrt{m_4^2+q^2},0,-q\sin(\theta),-q\cos(\theta))$ where q is determined through energy conservation $2p = \sqrt{m_3^2+q^2} + \sqrt{m_4^2+q^2}$.

A.4 Passarino-Veltman functions

To present our results we use the standard Passarino-Veltman functions [75]:

$$\begin{aligned} & C_{ij}(m_1,m_2,m_3) = \\ & \quad \int \frac{d^4k}{i\pi^2} \frac{1}{(k^2-m_1^2)((k+p_i)^2-m_2^2)((k+p_i+p_j)^2-m_3^2)} \\ & D_{ijk}(m_1,m_2,m_3,m_4) = \\ & \quad \int \frac{d^4k}{i\pi^2} \frac{1}{(k^2-m_1^2)((k+p_i)^2-m_2^2)((k+p_i+p_j)^2-m_3^2)((k+p_i+p_j+p_k)^2-m_4^2)} \end{aligned} \tag{A.21}$$

and introduce the following abbreviations

$$\begin{aligned} & C_{12} \equiv C_{12}(M,M,M) && C_{13} \equiv C_{13}(M,M,m) \\ & C_{14} \equiv C_{14}(M,M,m) && C_{23} \equiv C_{23}(M,M,m) \\ & C_{24} \equiv C_{24}(M,M,m) && C_{34} \equiv C_{34}(M,M,m) \\ & D_{123} \equiv D_{123}(M,M,M,m) && D_{132} \equiv D_{132}(M,M,m,m) \\ & D_{213} \equiv D_{213}(M,M,M,m)\,. \end{aligned} \tag{A.22}$$

The loss of information in the exact mass dependence of the C and D functions has to be taken into account when symmetrizing in m and M in formulae Eqs (A.17).

A.5 Additional plots

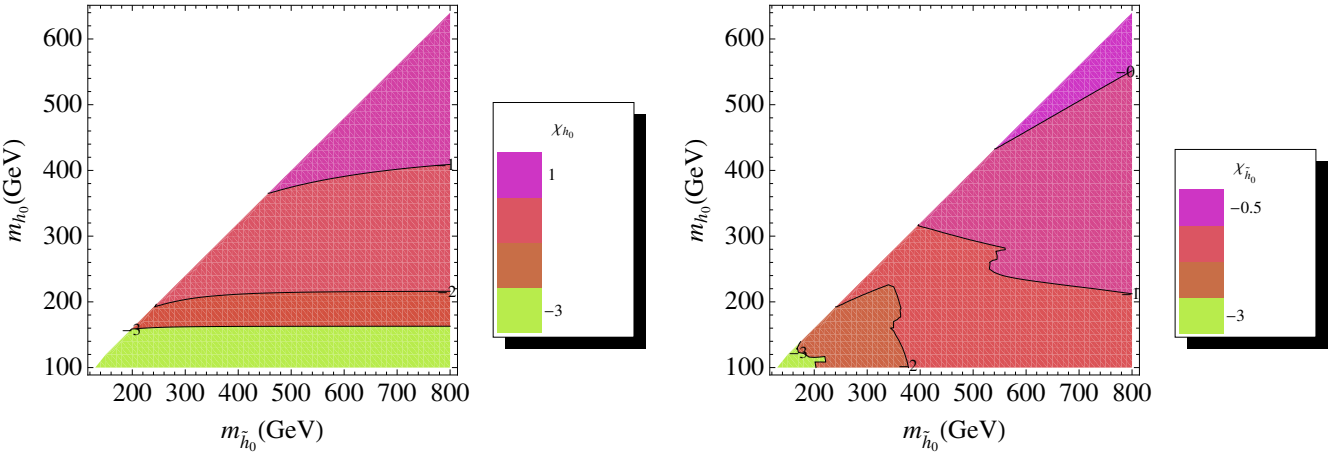

Figure 13. Contours plots of the ratio $\chi_{h_0} = \log\left(\frac{\Gamma_{h_0}}{m_{h_0}}\right)$ (right) of the h_0 and the ratio $\chi_{\tilde{h}_0} = \log\left(\frac{\Gamma_{\tilde{h}_0}}{m_{\tilde{h}_0}}\right)$ of the $\tilde{h}_0$.

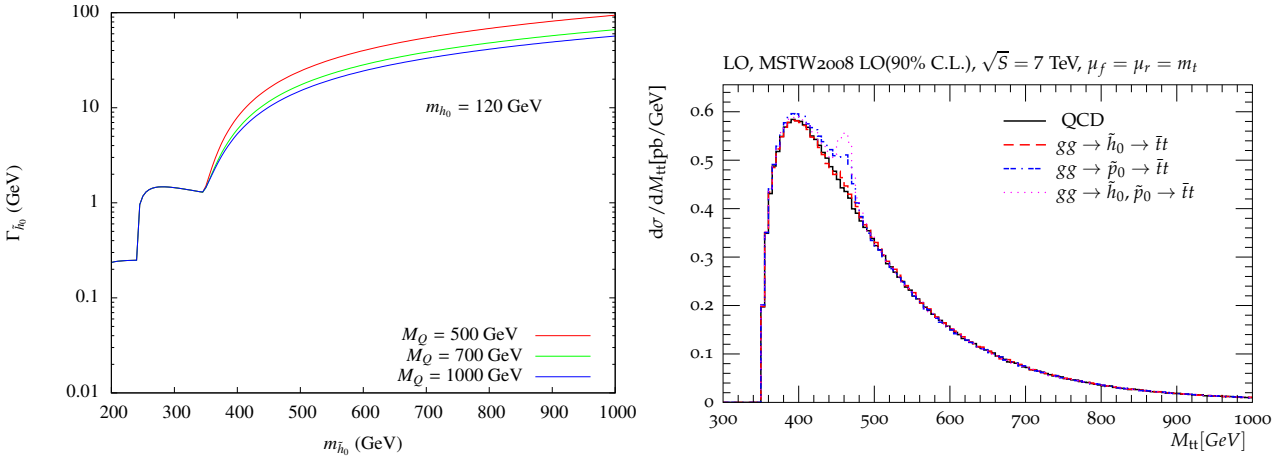

Figure 14. (left) Width $\Gamma_{\tilde{h}_0}$ as a function of mass, $m_{\tilde{h}_0}$, for $m_{h_0} = 120$ GeV, $M_2 = M_1 = 1$ TeV for different values of the fermion mass scale. (right) Histogram for $gg \to \bar{t}t$ for $\sqrt{S} = 7$ TeV with 5 GeV-bins.

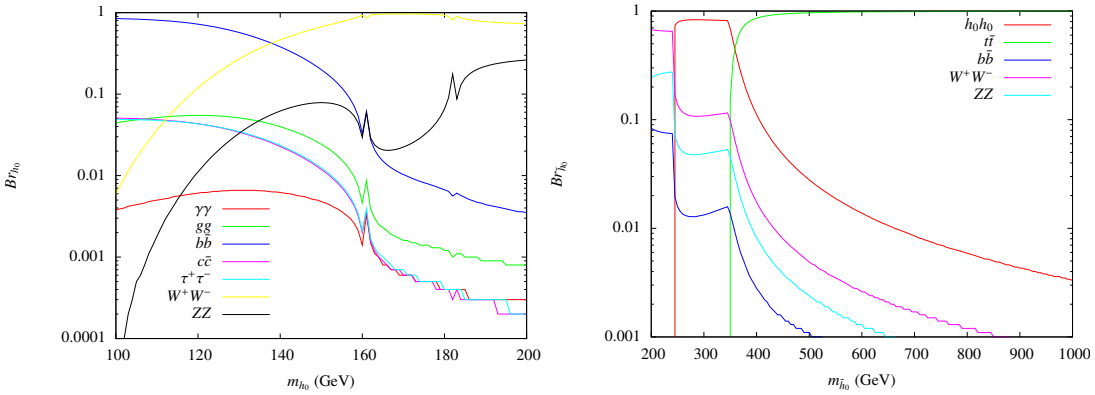

Figure 15. (left,right) Branching ratios Br_{h_0} and $\mathrm{Br}_{\tilde{h}_0}$ as a function of the masses m_{h_0} and $m_{\tilde{h}_0}$ and fixed $m_{\tilde{h}_0} = 120$ GeV and $m_{h_0} = 450$ GeV respectively for $M_2 = M_1 = 1$ TeV and $M_Q = 500$ GeV.

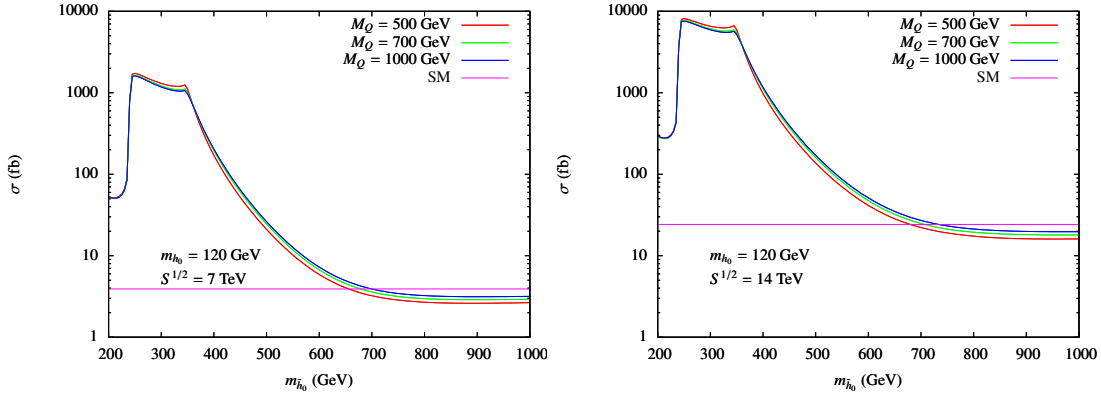

Figure 16. The cross section of $pp \to h_0h_0$ via gluon fusion at the LHC for $\sqrt{s} = 7/14$ TeV respectively versus the mass of the $\tilde{h}_0$, $m_{\tilde{h}_0}$, for $m_{h_0} = 120$ GeV. We note that the fermion mass scale $M_Q = M_u = M_d$ has very little influence on the results as emphasized in section 5. Note that for large $m_{\tilde{h}_0}$ the SM model value is approached by virtue of decoupling of the LW Higgs.

B Results for $gg \to h_0/\tilde{h}_0/\tilde{p}_0 \to \bar{t}t$

The amplitudes for the processes can directly be obtained from the ones from the double Higgs pair production in the previous section by suitable replacements. From the amplitude $gg \to h_0 \to h_0h_0$ in eq. (A.5), using eq.(2.14) and the definition of λ in the Higgs potential chosen in section 2.1 one obtains:

$$\mathcal{A}_0^{\triangle}(gg \to h_0(\tilde{h}_0) \to \bar{t}t) = s^2_{H-\tilde{H}}(g^t_{\mathrm{phys}})_{11}\Big(\frac{1}{s-m^2_{h_0}+im_{h_0}\Gamma_{h_0}} - \frac{1}{s-m^2_{\tilde{h}_0}-im_{\tilde{h}_0}\Gamma_{\tilde{h}_0}}\Big)\, s\ \tilde{F}_{1/2}[\bar{t}t]$$

Furthermore, from the $gg \to \tilde{p}_0 \to \tilde{p}_0h_0$ amplitude in eq. (A.8) one obtains:

$$\mathcal{A}_0^{\triangle,\tilde{p}_0}(gg \to \tilde{p}_0 \to \bar{t}t) = \Big(\frac{-2i(g^t_{\mathrm{phys}})_{11}}{s-m^2_{\tilde{p}_0}-im_{\tilde{p}_0}\Gamma_{\tilde{p}_0}}\, s\ \tilde{P}_{1/2}\Big)[\bar{t}\gamma_5 t] \tag{B.1}$$

Note, in both cases, we have not evaluated the spinors $t, \bar{t}$.

C Diagonalization of Mass Matrices

Here we shall describe a method for performing the hyperbolic diagonalization

$$\mathcal{M}_{t,\text{phys}}\eta_3 \;=\; S_R^\dagger\,\mathcal{M}_t\eta_3\,S_L \tag{C.1}$$

using similarity transformations for which standard tools, e.g. `Diag 1.3` [76], can be used, based on the observation that:

$$(S_{R/L}\eta_3)^{-1} = S_{R/L}^\dagger\eta_3 \tag{C.2}$$

The latter relation is easily verified from eq. (2.13)

Here we will describe a procedure of obtaining S_L and S_R numerically using routines provided. From there it is straightforward to verify that: First, we recognize that

$$\begin{aligned}\text{diag}(m^2_{t,\text{phys}}, m^2_{\tilde{t},\text{phys}}, m^2_{\tilde{T},\text{phys}}) &= \mathcal{M}_{t,\text{ph}}\eta_3\mathcal{M}^\dagger_{t,\text{ph}}\eta_3 \\ &= A_R(\eta_3\mathcal{M}_t\eta_3\mathcal{M}_t^\dagger)A_R^{-1} = A_L(\eta_3\mathcal{M}_t^\dagger\eta_3\mathcal{M}_t)A_L^{-1}\ .\end{aligned} \tag{C.3}$$

with $A_R \equiv S_R^\dagger\eta_3$ and $A_L \equiv \eta_3 S_L^\dagger$.

C.1 Mass sum rules

In this section we would like to point out some tree-level sum rules for matrices. When the matrices are diagonalized by hyperbolic rotations the trace remains an invariant. To be more precise suppose we had a matrix that is diagonalized as follows

$$\mathcal{M}_{\text{phys}}\,\eta = S^\dagger\,\mathcal{M}\eta\,S\ , \tag{C.4}$$

with

$$S^\dagger\eta S = \eta\ , \qquad \mathcal{M}_{\text{phys}} = \text{diag}(m^2_{a,\text{phys}}, m^2_{b,\text{phys}}, ...)\ , \tag{C.5}$$

then

$$\text{tr}[\mathcal{M}_{\text{phys}}] = \text{tr}[\mathcal{M}]\ . \tag{C.6}$$

The correctness of (C.6) can be immediately verified using the properties above. The diagonalization can be interpreted as a symmetry transformation where η plays the role of the metric. Thus the statement eq. (C.6) is nothing but the fact that the trace of the $(2,0)$-tensor $(M\eta)_{\alpha\beta}$ is an invariant; $M_\alpha{}^\alpha = \text{tr}[M]$. Thus one can deduce sum rules for the masses. Applied to the CP-even Higgs sector the RHS follows from writing (2.4) in matrix form, c.f. [26] and the LHS is given by definition

$$m^2_{h_0,\text{phys}} + m^2_{\tilde{h}_0} = M_H^2 = (m^2_{\tilde{p}_0,\text{phys}})\ . \tag{C.7}$$

The correctness is readily verified from eq. (2.4). Note, with the peculiar fact that at tree-level $m^2_{\tilde{p}_0,\text{phys}} = M_H^2$ equation (5.1) follows. This technique applies to the entire bosonic sector. For the neutral gauge bosons one gets

$$m^2_{\tilde{A},\text{phys}} + m^2_{Z,\text{phys}} + m^2_{\tilde{Z},\text{phys}} = M_1^2 + M_2^2 \tag{C.8}$$

with $M_{1,2}$ the mass scale of the $U(1)_Y$ and $SU(2)_L$ HD gauge terms respectively. The field $\tilde{A}$ is the LW-partner of the photon. Note the photon is not explicitly written down since it remains massless. eq. (C.8) is consistent with the result for $M_1 = M_2$ in appendix B of reference [24].

The fermions are slightly more complicated as they proceed via a bi-unitary hyperbolic diagonalization. The statement is that:

$$\text{diag}(m^2_{t,\text{phys}}, m^2_{\tilde{t},\text{phys}}, m^2_{\tilde{T},\text{phys}}) \equiv \text{tr}[\mathcal{M}_{t,\text{ph}}\eta_3\mathcal{M}^\dagger_{t,\text{ph}}\eta_3] = \text{tr}[\mathcal{M}_t\eta_3\mathcal{M}^\dagger_t\eta_3] \,, \tag{C.9}$$

which follows immediately from the eq. (C.3). Applied to the fermions we get:

$$m^2_{t,\text{phys}} + m^2_{\tilde{t},\text{phys}} + m^2_{\tilde{T},\text{phys}} = M^2_u + M^2_Q \,, \tag{C.10}$$

where eq. (2.11) was invoked for $\mathcal{M}_t$. The correctness of this equation can be verified for the explicit result given in chapter 2.3.2. of reference [26] to each order in the expansion. In chapter 3 of reference [26] similar consideration were taken into account to show the absence of quadratic divergences in the top-loop in the AF formalism.

We would like to emphasize that the trace formula (C.6) and (C.9) are general and in particular apply in each order of perturbation theory but the specific evaluation we have given in Eqs (C.7),(C.8) and (C.10) have made use of the trace at tree-level and are thus subject to corrections.

C.2 Spurious phases

Furthermore we consider it worthwhile to discuss the freedom of reparametrizing phases in the mass and Yukawa matrix of the LWSM. Note that the Yukawa matrix presented in ref. [26] contains imaginary entries and one might therefore wonder whether they are associated with CP-violation or whether they are unphysical/spurious phases. For fixed flavour there are six fermion in each LW-generation counting left and right handed field separately. The freedom of choosing their spurious phases is reflected in the fact that the matrices A_L and A_R are determined by eq.(C.3) up to

$$A_R \to \text{diag}(e^{iR_1}, e^{iR_2}, e^{iR_3})A_R \,, \quad A_L \to \text{diag}(e^{iL_1}, e^{iL_2}, e^{iL_3})A_L \tag{C.11}$$

a multiplicative diagonal unitary matrix. Rewriting eq.(C.1) as

$$\mathcal{M}_{t,\text{phys}}\eta_3 \;= A_R(\eta_3\mathcal{M}_t\eta_3)A_L^{-1} \tag{C.12}$$

we see that choosing the fermion masses to be real and positive (or negative) fixes the differences $R_i - L_i$ for $i = 1, 2, 3$. Writing $L_1 = L_1, L_2 = L_1 + \Delta_2, L_3 = L_1 + \Delta_3$ it is noticed, as usual, that only the two parameters Δ_2 and Δ_3 lead to a change in the entries of $g_{t,\text{phys}}$; two arbitrary phases. This freedom can be used to reparametrize the third LW-generation by $e^{iR_3} = e^{iL_3} = i$ the Yukawa matrix $g_{t,\text{phys}}$ in ref. [26] to render its entries completely real.

To this end we would like to note that we find that $g_{t,\text{phys}}$ is smooth in the limit $M_Q \to M_u$ contrary to a remark made in the appendix of ref. [77]. Note in their explicit

formula these authors present an expansion in $1/(M_u - M_Q)$ which cannot be compared with the expansion in $1/M_u$ for $M_u = M_Q$ presented in ref. [26] of as the former is singular in the degenerate limit. The fact that their expansion does not have imaginary parts can be explained by the freedom of phase reparametrization discussed above.

References

[1] B. Grinstein, D. O'Connell, M. B. Wise, "The Lee-Wick standard model," Phys. Rev. **D77** (2008) 025012. [arXiv:0704.1845 [hep-ph]].

[2] T. D. Lee and G. C. Wick, "Negative Metric and the Unitarity of the S Matrix," Nucl. Phys. B **9** (1969) 209.

[3] T. D. Lee and G. C. Wick, "Finite Theory of Quantum Electrodynamics," Phys. Rev. D **2** (1970) 1033.

[4] T. D. Lee, *in Proceedings of the International School of Physics "Ettore Majorana," Erice, Italy, 1970, edited by A. Zichichi, New York, 1971, 63-93*

[5] S. Coleman, "Acausality," *in *Erice 1969, Ettore Majorana School On Subnuclear Phenomena*, New York 1970, 282-327*

[6] B. Grinstein, D. O'Connell, M. B. Wise, "Causality as an emergent macroscopic phenomenon: The Lee-Wick O(N) model," Phys. Rev. **D79** (2009) 105019. [arXiv:0805.2156 [hep-th]].

[7] R. E. Cutkosky, P. V. Landshoff, D. I. Olive and J. C. Polkinghorne, "A non-analytic S matrix," Nucl. Phys. B **12** (1969) 281.

[8] E. Alvarez, L. Da Rold, C. Schat, A. Szynkman, "Vertex Displacements for Acausal Particles: Testing the Lee-Wick Standard Model at the LHC," JHEP **0910** (2009) 023. [arXiv:0908.2446 [hep-ph]].

[9] D. G. Boulware and D. J. Gross, "Lee-Wick Indefinite Metric Quantization: A Functional Integral Approach," Nucl. Phys. B **233** (1984) 1.

[10] A. van Tonder, M. Dorca, "Non-perturbative Quantization of Phantom and Ghost Theories: Relating Definite and Indefinite Representations," Int. J. Mod. Phys. A **22** (2007) 2563 [arXiv:hep-th/0610185].

[11] A. van Tonder, "Unitarity, Lorentz invariance and causality in Lee-Wick theories: An Asymptotically safe completion of QED," [arXiv:0810.1928 [hep-th]].

[12] B. Fornal, B. Grinstein, M. B. Wise, "Lee-Wick Theories at High Temperature," Phys. Lett. **B674** (2009) 330-335. [arXiv:0902.1585 [hep-th]].

[13] B. Grinstein, D. O'Connell and M. B. Wise, "Massive Vector Scattering in Lee-Wick Gauge Theory," Phys. Rev. D **77** (2008) 065010 [arXiv:0710.5528 [hep-ph]].

[14] J. R. Espinosa, B. Grinstein, D. O'Connell, M. B. Wise, "Neutrino masses in the Lee-Wick standard model," Phys. Rev. **D77** (2008) 085002. [arXiv:0705.1188 [hep-ph]].

[15] B. Grinstein, D. O'Connell, "One-Loop Renormalization of Lee-Wick Gauge Theory," Phys. Rev. **D78** (2008) 105005. [arXiv:0801.4034 [hep-ph]].

[16] J. R. Espinosa, B. Grinstein, "Ultraviolet Properties of the Higgs Sector in the Lee-Wick Standard Model," Phys. Rev. **D83** (2011) 075019. [arXiv:1101.5538 [hep-ph]].

[17] C. D. Carone, R. F. Lebed, "A Higher-Derivative Lee-Wick Standard Model," JHEP **0901** (2009) 043. [arXiv:0811.4150 [hep-ph]].

[18] C. D. Carone, "Higher-Derivative Lee-Wick Unification," Phys. Lett. **B677** (2009) 306-310. [arXiv:0904.2359 [hep-ph]].

[19] A. Rodigast, T. Schuster, "No Lee-Wick Fields out of Gravity," Phys. Rev. **D79** (2009) 125017. [arXiv:0903.3851 [hep-ph]].

[20] Y. -F. Cai, T. -t. Qiu, R. Brandenberger, X. -m. Zhang, "A Nonsingular Cosmology with a Scale-Invariant Spectrum of Cosmological Perturbations from Lee-Wick Theory," Phys. Rev. **D80** (2009) 023511. [arXiv:0810.4677 [hep-th]].

[21] T. G. Rizzo, "Searching for Lee-Wick Gauge Bosons at the LHC," JHEP **0706** (2007) 070 [arXiv:0704.3458 [hep-ph]].

[22] T. G. Rizzo, "Unique Identification of Lee-Wick Gauge Bosons at Linear Colliders," JHEP **0801** (2008) 042 [arXiv:0712.1791 [hep-ph]].

[23] T. R. Dulaney and M. B. Wise, "Flavor Changing Neutral Currents in the Lee-Wick Standard Model," arXiv:0708.0567 [hep-ph].

[24] T. E. J. Underwood and R. Zwicky, "Electroweak Precision Data and the Lee-Wick Standard Model," Phys. Rev. D **79** (2009) 035016 [arXiv:0805.3296 [hep-ph]].

[25] R. S. Chivukula, A. Farzinnia, R. Foadi, E. H. Simmons, "Custodial Isospin Violation in the Lee-Wick Standard Model," Phys. Rev. **D81** (2010) 095015. [arXiv:1002.0343 [hep-ph]].

[26] F. Krauss, T. E. J. Underwood and R. Zwicky, "The process $gg \to h_0 \to \gamma\gamma$ in the Lee-Wick Standard Model," Phys. Rev. D **77** (2008) 015012 [arXiv:0709.4054 [hep-ph]].

[27] C. D. Carone, R. Primulando, "Constraints on the Lee-Wick Higgs Sector," Phys. Rev. **D80** (2009) 055020. [arXiv:0908.0342 [hep-ph]].

[28] G. Cacciapaglia, A. Deandrea, J. Llodra-Perez, "Higgs —¿ Gamma Gamma beyond the Standard Model," JHEP **0906** (2009) 054. [arXiv:0901.0927 [hep-ph]].

[29] E. Alvarez, E. C. Leskow, J. Zurita, "Collider Bounds on Lee-Wick Higgs Bosons," [arXiv:1104.3496 [hep-ph]].

[30] M. J. G. Veltman, "Second Threshold In Weak Interactions," Acta Phys. Polon. B **8** (1977) 475.

[31] T. Aaltonen *et al.* [CDF Collaboration], "Invariant Mass Distribution of Jet Pairs Produced in Association with a W boson in $p\bar{p}$ Collisions at $\sqrt{s} = 1.96$ TeV," Phys. Rev. Lett. **106** (2011) 171801 [arXiv:1104.0699 [hep-ex]].

[32] U. Baur, T. Plehn, D. L. Rainwater, "Probing the Higgs selfcoupling at hadron colliders using rare decays," Phys. Rev. **D69** (2004) 053004. [hep-ph/0310056].

[33] T. Plehn, M. Spira, P. M. Zerwas, "Pair production of neutral Higgs particles in gluon-gluon collisions," Nucl. Phys. **B479** (1996) 46-64. [arXiv:hep-ph/9603205 [hep-ph]].

[34] D. Dicus, A. Stange, S. Willenbrock, "Higgs decay to top quarks at hadron colliders," Phys. Lett. **B333** (1994) 126-131. [hep-ph/9404359].

[35] R. Barcelo, M. Masip, "Extra Higgs bosons in $t\bar{t}$ production at the LHC," Phys. Rev. **D81** (2010) 075019. [arXiv:1001.5456 [hep-ph]].

[36] K. Nakamura et al. (Particle Data Group), J. Phys. G 37, 075021 (2010)

[37] E. W. N. Glover and J. J. van der Bij, *HIGGS BOSON PAIR PRODUCTION VIA GLUON FUSION*, *Nucl. Phys.* **B309** (1988) 282.

[38] T. Plehn, G. P. Salam, M. Spannowsky, "Fat Jets for a Light Higgs," Phys. Rev. Lett. **104** (2010) 111801. [arXiv:0910.5472 [hep-ph]].

[39] U. Baur, L. H. Orr, "Searching for $t\bar{t}$ Resonances at the Large Hadron Collider," Phys. Rev. **D77** (2008) 114001. [arXiv:0803.1160 [hep-ph]].

[40] U. Baur, L. H. Orr, "High p_T Top Quarks at the Large Hadron Collider," Phys. Rev. **D76** (2007) 094012. [arXiv:0707.2066 [hep-ph]].

[41] V. Barger, T. Han, D. G. E. Walker, "Top Quark Pairs at High Invariant Mass: A Model-Independent Discriminator of New Physics at the LHC," Phys. Rev. Lett. **100** (2008) 031801. [hep-ph/0612016].

[42] D. E. Kaplan, K. Rehermann, M. D. Schwartz, B. Tweedie, "Top Tagging: A Method for Identifying Boosted Hadronically Decaying Top Quarks," Phys. Rev. Lett. **101** (2008) 142001. [arXiv:0806.0848 [hep-ph]].

[43] A. Abdesselam, E. B. Kuutmann, U. Bitenc, G. Brooijmans, J. Butterworth, P. Bruckman de Renstrom, D. Buarque Franzosi, R. Buckingham *et al.*, "Boosted objects: A Probe of beyond the Standard Model physics," Eur. Phys. J. **C71** (2011) 1661. [arXiv:1012.5412 [hep-ph]].

[44] R. Frederix, F. Maltoni, "Top pair invariant mass distribution: A Window on new physics," JHEP **0901** (2009) 047. [arXiv:0712.2355 [hep-ph]].

[45] K. J. Peters, "A Primer on partial wave analysis," Int. J. Mod. Phys. **A21** (2006) 5618-5624. [hep-ph/0412069].

[46] M. Harada, F. Sannino, J. Schechter, "Simple description of pi pi scattering to 1-GeV," Phys. Rev. **D54** (1996) 1991-2004. [hep-ph/9511335].

[47] T. Aaltonen *et al.* [CDF Collaboration], "Evidence for a Mass Dependent Forward-Backward Asymmetry in Top Quark Pair Production," Phys. Rev. **D83** (2011) 112003. [arXiv:1101.0034 [hep-ex]].

[48] D. Collaboration, "Forward-backward asymmetry in top quark-antiquark production," arXiv:1107.4995 [hep-ex].

[49] Q. -H. Cao, D. McKeen, J. L. Rosner, G. Shaughnessy, C. E. M. Wagner, "Forward-Backward Asymmetry of Top Quark Pair Production," Phys. Rev. **D81** (2010) 114004. [arXiv:1003.3461 [hep-ph]].

[50] A. D. Martin, W. J. Stirling, R. S. Thorne and G. Watt, "Parton distributions for the LHC," Eur. Phys. J. C **63** (2009) 189 [arXiv:0901.0002 [hep-ph]].

[51] S. Dawson, S. Dittmaier, M. Spira, "Neutral Higgs boson pair production at hadron colliders: QCD corrections," Phys. Rev. **D58** (1998) 115012. [hep-ph/9805244].

[52] T. Hahn, "Generating Feynman diagrams and amplitudes with FeynArts 3," Comput. Phys. Commun. **140** (2001) 418-431. [hep-ph/0012260].

[53] A. V. Semenov, "LanHEP: A Package for automatic generation of Feynman rules in field theory. Version 2.0," [hep-ph/0208011].

[54] T. Hahn, M. Perez-Victoria, "Automatized one loop calculations in four-dimensions and D-dimensions," Comput. Phys. Commun. **118** (1999) 153-165. [hep-ph/9807565].

[55] G. Aad *et al.* [The ATLAS Collaboration], "Expected Performance of the ATLAS Experiment - Detector, Trigger and Physics," [arXiv:0901.0512 [hep-ex]].

[56] E. Cogneras and D. Pallin, "Generic $t\bar{t}$ resonance search with the ATLAS detector", ATL-PHYS-PUB-2006-033. ATL-COM-PHYS-2006-054.

[57] G. Azuelos, D. Cavalli, H. Przysiezniak and L. Vacavant, "Search for the radion using the ATLAS detector," Eur. Phys. J. direct C **4** (2002) 16.

[58] S. Gennai, "Search for the radion decay into a Higgs boson pair with gamma gamma + b b, tau tau + b b and b b + b b final states," Czech. J. Phys. **55** (2005) B137.

[59] D. Dominici, G. Dewhirst, S. Gennai, L. Fano and A. Nikitenko, "Search for the radion decay $\phi \to HH$ with gamma gamma + B anti-B, tau tau + B anti-B and B anti-B + B anti-B final states in CMS," *Prepared for Lake Louise Winter Institute 2004 on Fundamental Interactions (LL WI 2004), Lake Louise, Alberta, Canada, 15-21 Feb 2004*

[60] E. Richter-Was, D. Froidevaux, F. Gianotti, L. Poggioli, D. Cavalli and S. Resconi, "Minimal supersymmetric standard model Higgs rates and backgrounds in ATLAS," Int. J. Mod. Phys. A **13** (1998) 1371.

[61] M. Bowen, Y. Cui, J. D. Wells, "Narrow trans-TeV Higgs bosons and $H \to hh$ decays: Two LHC search paths for a hidden sector Higgs boson," JHEP **0703** (2007) 036. [hep-ph/0701035].

[62] The ATLAS Collaboration, "Combined Standard Model Higgs Boson Searches in pp Collisions at $\sqrt{s} = 7$ TeV with the ATLAS Experiment at the LHC", ATLAS-CONF-2011-112.

[63] The CMS Collaboration, "Search for standard model Higgs boson in pp collisions at $\sqrt{s} = 7$ TeV", CMS-PAS-HIG-11-011.

[64] B. Altunkaynak, M. Holmes, P. Nath, B. D. Nelson, G. Peim, "SUSY Discovery Potential and Benchmarks for Early Runs at $\sqrt{s} = 7$ TeV at the LHC," Phys. Rev. **D82** (2010) 115001. [arXiv:1008.3423 [hep-ph]].

[65] T. Gleisberg, S. Hoeche, F. Krauss, M. Schonherr, S. Schumann, F. Siegert and J. Winter, "Event generation with SHERPA 1.1," JHEP **0902**, 007 (2009) [arXiv:0811.4622 [hep-ph]].

[66] S. Schumann and F. Krauss, "A Parton shower algorithm based on Catani-Seymour dipole factorisation," JHEP **0803**, 038 (2008) [arXiv:0709.1027 [hep-ph]].

[67] M. Schonherr and F. Krauss, "Soft Photon Radiation in Particle Decays in SHERPA," JHEP **0812** (2008) 018 [arXiv:0810.5071 [hep-ph]].

[68] S. Hoeche, F. Krauss, S. Schumann and F. Siegert, "QCD matrix elements and truncated showers," JHEP **0905**, 053 (2009) [arXiv:0903.1219 [hep-ph]].

[69] F. Krauss, R. Kuhn and G. Soff, "AMEGIC++ 1.0: A Matrix element generator in C++," JHEP **0202**, 044 (2002) [arXiv:hep-ph/0109036].

[70] T. Gleisberg and S. Hoeche, "Comix, a new matrix element generator," JHEP **0812**, 039 (2008) [arXiv:0808.3674 [hep-ph]].

[71] A. Buckley, J. Butterworth, L. Lonnblad, H. Hoeth, J. Monk, H. Schulz, J. E. von Seggern, F. Siegert *et al.*, "Rivet user manual," [arXiv:1003.0694 [hep-ph]].

[72] M. Cacciari and G. P. Salam, "Dispelling the N^3 myth for the k_t jet-finder," Phys. Lett. B **641** (2006) 57 [arXiv:hep-ph/0512210].

[73] A. Belyaev, M. Drees, O. J. P. Eboli, J. K. Mizukoshi, S. F. Novaes, Phys. Rev. **D60** (1999) 075008. [hep-ph/9905266].

[74] R. Mertig, M. Bohm, A. Denner, "FEYNCALC: Computer algebraic calculation of Feynman amplitudes," Comput. Phys. Commun. **64** (1991) 345-359.

[75] G. Passarino, M. J. G. Veltman, "One Loop Corrections for e+ e- Annihilation Into mu+ mu- in the Weinberg Model," Nucl. Phys. **B160** (1979) 151.

[76] T. Hahn,"Routines for the diagonalization of complex matrices," [physics/0607103].

[77] E. Alvarez, L. Da Rold, C. Schat and A. Szynkman, "Electroweak precision constraints on the Lee-Wick Standard Model," JHEP **0804** (2008) 026 [arXiv:0802.1061 [hep-ph]].